EFFICIENT OPERATION OF VARIABLE-POLE INDUCTION MACHINES AND DRIVES

BY

ELIE LIBBOS

THESIS

Submitted in partial fulfillment of the requirements
for the degree of Master of Science in Electrical and Computer Engineering
in the Graduate College of the
University of Illinois at Urbana-Champaign, 2020

Urbana, Illinois

Adviser:

Assistant Professor Arijit Banerjee

ABSTRACT

Transportation electrification is a necessary step for a sustainable and clean energy future. As land vehicles and trucks are responsible for 82% of transportation emissions, electric vehicles (EVs) must become more affordable to replace conventional cars and reduce emissions. High power density, high efficiency, inexpensive drivetrains operating over a wide torque/speed range are critical for EVs. Most modern EVs use permanent magnet (PM) motors which rely on rare-earth material to achieve high energy efficiency. However, rare-earth magnets are expensive, have low recycling rates, and have high risk of price volatility. An induction machine (IM) is a magnet-free motor which offers a cost-effective, rugged and reliable alternative to permanent magnet motors. IMs have been widely established in EVs and are still used in modern designs. The magnetic pole count of an IM can be electronically varied by controlling a high number of stator currents as the cage-rotor naturally follows the stator. Variable-pole operation extends the speed range of an IM, a feature which is attractive in EV applications. Conventionally, pole count has been linked only to the machine operating speed, with a high pole at low speed and low pole at high speed. In this thesis, we show that pole count is a degree of freedom that can be used to improve drivetrain efficiency. Pole count must be selected based on both the required torque and operating speeds if the goal is to minimize losses or stator current. Low pole counts are more efficient than high pole counts at producing low and intermediate torque levels. By exploiting this property, experimental average power loss reduction and torque-per-ampere improvements of 1/3 and 2X were achieved at partial loading condition, where an EV operates for a predominant period of the time. We also show that power electronics converters for variable-pole IMs are more efficient than 3-phase fixed-pole converters.

To my parents, for their love and support.

ACKNOWLEDGMENTS

First of all, I would like to acknowledge my family, Ghassan, Rita, Amanda, Michel and Buffi, for their endless support and love. Without my parent's sacrifices, it would have been impossible for me to be the person I am today. With their support, I can overcome any obstacle in life. Making them proud of me is the most amazing feeling in the world.

I am grateful for my adviser, Dr. Arijit Banerjee, for his patience, guidance and endless support, and for always believing in me. He has always been there to support me. His passion for research and innovation has motivated me to think outside of the box and see things differently. I am honored to be part of his research group. Dr. Banerjee is a role model to me. I have learned from him not only about conducting research and understanding theory, but also about leadership and perseverance. I am so excited to start my doctoral studies, as I feel that I have a lot more to learn and explore. I am forever thankful for the amazing opportunities he has given me. Joining his research group changed my life forever and made me a better engineer and person.

I am thankful for Dr. Philip T. Krein for his support and valuable feedback on my research project. He has helped me improve the quality of my research work and publications. I would like to thank Dr. Matthew P. Magill who designed and built the experimental machine I used in my research. His thesis work on pole-changing induction machines motivated me to work on this topic.

I am thankful for Bonhyun Ku, Shivang Agrawal and Phuc Huynh for their endless support and for helping me in my research. The Banerjee Research Group is like a family to me. The group dynamics made my grad school experience amazing. I would like to thank Ruomu Hao for his amazing work on writing the FPGA software. His passion, dedication and perseverance are truly appreciated. I had so much fun debugging hardware/software issues with Ruomu. I would like to thank Samira Tungare for her work on finite

element analysis simulations.

I am grateful to the Power and Energy Systems students and staff. I love the group spirit and enjoy the activities and fun events with them. I am so proud to be a part of this group. We have some amazing memories together. I want to thank Joyce Mast for her support in technical writing of publications. I thank Robin Smith for her work on paperwork and conference travel. I am thankful to Kevin Colravy for his support in the laboratory.

I am thankful to my fantastic mentors who inspired me to pursue graduate studies in power and energy. Most of my knowledge in power and energy started by enrolling in Dr. Sami Karaki's classes at the American University of Beirut (AUB). I will forever be thankful to Dr. Karaki. His class on power electronics inspired me to apply for my first power electronics research internship at the University of Connecticut. I am grateful for Dr. Ali M. Bazzi who gave me a life-changing opportunity to intern at his lab. Right after the internship, I knew that I wanted do research in power electronics, and electric machines and drives, for the rest of my life. I have learned so much from Dr. Bazzi and I am forever grateful for the opportunities he gave me.

Finally, I would like to thank the Grainger Center for Electric Machinery and Electromechanics and the Power Optimization of Electro-Thermal Systems (POETS) NSF Engineering Research Center at the University of Illinois for funding the project. I would also like to thank the ECE department for the ECE Distinguished Research Fellowship.

TABLE OF CONTENTS

LIST OF TABLES

LIST OF FIGURES

CHAPTER 1

INTRODUCTION

Land vehicles and trucks are responsible for 82% of the transportation sector greenhouse gases emissions [1]. Electrifying land transportation is a promising step towards a sustainable low emission future [2]. Electric vehicles (EVs) reduce emissions by roughly 15 % compared to internal combustion engine (ICE) cars. The emission gap between ICE cars and EVs is expected to become larger with the increase of clean energy [3]. However, EV sales are still low compared to ICE cars as less than 3 % of cars purchased in the U.S in 2019 are electric [4]. Energy efficient and cost effective electric motors, drives and batteries are needed for EVs to compete with conventional cars.

Currently, permanent magnet (PM) synchronous motors are the most popular in traction applications because of their high power density and efficiency [5]. However, the major problem of PM technologies is the usage of rare-earth

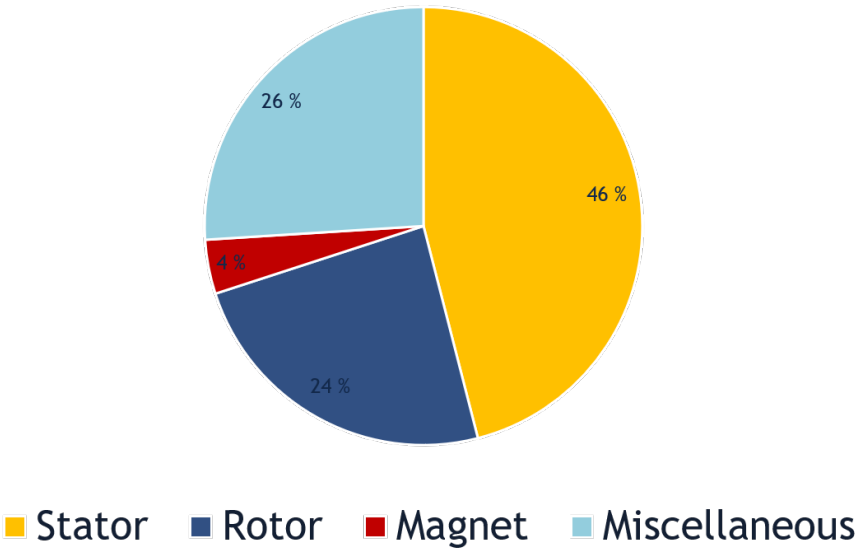

Figure 1.1: U.S. Department of Energy 2025 EV electric motor cost breakdown targets [7].

magnets which are expensive, have low recycling rates, and have high risk of price volatility [6]. The U.S. Department of Energy (DOE) is pushing to reduce rare-earth magnet usage in its 2025 EV drivetrain targets [7]. Figure 1.1 shows the DOE 2025 cost breakdown targets of an EV electric motor. The magnet cost target is limited to 4 % of the total motor material cost, while rare-earth magnets exceed 50 % of a typical PM motor cost [8]. To meet these targets, designers have three alternatives: 1) reducing the usage of rare-earth magnets, 2) replacing rare-earth with ferrite magnets, or 3) using motors which are inherently magnet-free like induction machines (IMs) and synchronous reluctance machines (SRMs) [6, 9].

IMs are the main competitor to PM motors as they are the second most widely used motors in EVs [5]. IMs are fully established as viable alternatives for EVs [10, 11, 12] and are still being used in modern designs like the 2019 Audi e-tron [13]. IMs have advantages over PM motors in terms of ruggedness, fault tolerance, reliability, high overload capability, and cost effectiveness. Although PM motors have a higher peak efficiency than IMs, IMs can match PM motor efficiency in actual driving scenarios [11]. Power dense designs can be achieved with IMs because EV motors operate at high speeds. Unlike PM motors, the magnetic pole count of an IM is not constrained by any physical magnet and can be changed on-the-fly [14, 15, 16].

Fundamentally, torque capability of a machine is determined by the air-gap flux density, surface current density and machine dimensions irrespective of the magnetic pole count. However, operational torque capability can be improved by varying the pole count [15]. For example, the red-dashed curve in Fig. 1.2 shows a typical torque-speed characteristic of a six-pole IM. Beyond the base speed, denoted by ω_b in Fig. 1.2, the machine undergoes flux-weakening due to a limited dc-link voltage that feeds the power electronics converter. At high speeds beyond ω_b, the machine torque capability is eventually limited by its breakdown torque. Designing fixed-pole IMs with minimal leakage inductance and overmodulated power electronics improves high-speed torque capability at the cost of efficiency and power density [12, 17, 18]. Alternatively, if the same six-pole machine of Fig. 1.2 can be reconfigured on-the-fly to a lower pole count, such as four or two, its high-speed torque capability is improved by pushing the effective base speed to higher speeds, making it attractive for EVs, which require a wide operating speed range.

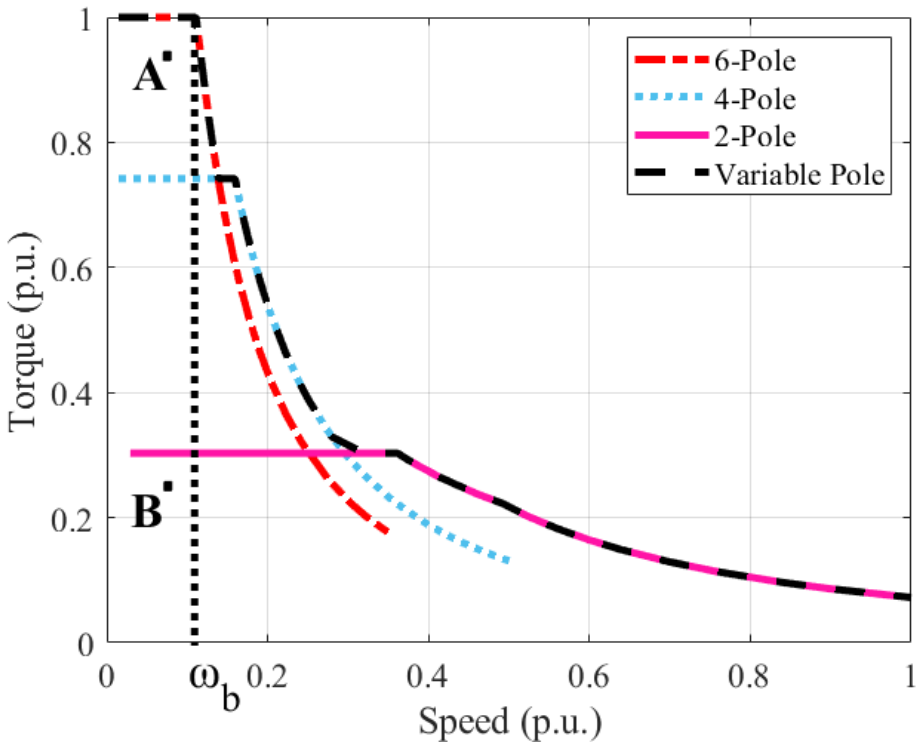

Figure 1.2: Torque-speed characteristics for 2-, 4-, and 6- pole configurations of a given IM as obtained from finite element analysis. The machine is nominally designed for 6-pole. ω_b is the 6-pole base speed. At high speeds beyond ω_b, switching to lower pole counts such as four and two improves operational torque capability.

Prior research has shown that variable-pole IMs can meet the requirements of wide speed range applications by utilizing a high pole count at low speeds and low pole count at high speeds [14, 15, 16, 19, 20, 21]. The authors of [16] designed a variable-pole IM for an automotive integrated starter to deliver high starting torque while still maintaining a cruising torque capability at high speeds. One of the most comprehensive pole-changing works, presented in [14, 20], explores the effect of winding and inverter configuration on pole-changing. In [15, 19], a 4-/2-pole IM was designed to maintain its rated power capability over a wide speed-range. To date, the operating pole count is solely based on operating speed irrespective of the torque required. In other words, the machine is always assumed to be delivering the rated torque and the pole count with the highest torque capability is selected at each speed. However, this assumption is rarely valid for EVs. In any realistic drive cycle, the machine delivers a partial torque most of the time and is

rarely used at its full rated capability [22, 23]. Therefore, it is crucial to select the operating pole count based on both torque and speed to maximize operational efficiency. To illustrate, consider the operating points A and B in Fig. 1.2. Both A and B are at the same speed but only a small torque is required at point B compared to A. At point A, it is easy to select the pole count based on the methods established in the literature as only 6-pole has enough torque capability. However, all pole configurations can deliver the torque required at point B. This thesis proposes a method of selecting the pole count to improve the operational efficiency of the variable-pole IMs over the entire torque/speed range [24, 25]. The effect of pole-changing on the design, efficiency and size of the multiphase converter driving the variable-pole IM is also investigated [26]. The major contributions of this thesis are:

- A pole-selection method is proposed for variable-pole IMs that takes into consideration both torque and speed. The pole count is seen as a degree of freedom that can be used to optimize an objective function. This work has been published in [24] and accepted for publication in [25].

- A steady-state "per-slot" model that explicitly considers each slot current is developed [24, 25]. The model works for all pole-changing techniques and captures any n-phase/p-pole excitation. The model is used to analyze the effect of pole count on the variable-pole IM current, voltage and magnetic flux.

- The pole count is used as a decision variable to maximize drivetrain efficiency and minimize stator current over the wide operating torque/speed range of an EV motor [24, 25].

- Variable-pole IMs require a co-design of the machine stator winding and power electronics converter. As a high number of power electronics ac ports is needed to vary the IM pole count [14], this thesis investigates the effect of the number of ac ports on the converter efficiency and its dc link capacitor sizing [26]. It also explores how varying the IM pole count benefits and constrains the drive design and operation. This work has been accepted for publication in [26].

Chapter 2 explains electronic pole-changing from both machine and power electronics perspectives. Chapter 3 shows the effects of pole count on current

and flux density. A generalized "per-slot" model that explicitly captures pole count p is derived and is the basis of the analysis used in this thesis. Chapter 4 explains how to select the IM pole count by considering both required torque and operating speed. An optimization seeks the pole count that minimizes an objective function. Strategies such as maximum torque per ampere (MTPA) and minimum loss operation are implemented for the variable-pole IM. The goal of these strategies is to select the pole count that minimizes power losses and stator current. Chapter 5 investigates power electronics converter design for variable-pole IMs. Efficiency and dc link capacitor sizing of drive are considered. A variable-pole IM requires a high number of ac ports in the power electronics converter. A higher number of power electronics devices reduces voltampere (VA) rating of each device. Thus, chapter 5 essentially compares two design strategies, namely, using either a low number of power electronics semiconductors with high VA rating or a high number devices with low VA rating. Chapter 6 presents the experimental setup which consists of a toroidally wound IM driven by an 18-phase GaN-based drive. Experimental results are provided to validate the analysis. Chapter 7 summarizes the thesis and outlines future work.

CHAPTER 2

ELECTRONIC POLE-CHANGING

The main goal of this chapter is to explain how an IM magnetic pole count can be varied. Both the machine and power electronics perspectives are considered. The analysis assumes a cage-rotor IM. In a squirrel-cage IM, the rotor pole count naturally follows the stator and is not constrained by any magnet [27]. Thus, the pole count of the IM is determined by the stator excitation. Changing the pole count of a PM machine requires magnet re-excitation [28], which is not feasible in EVs. Part of this chapter has been accepted for publication in [26].

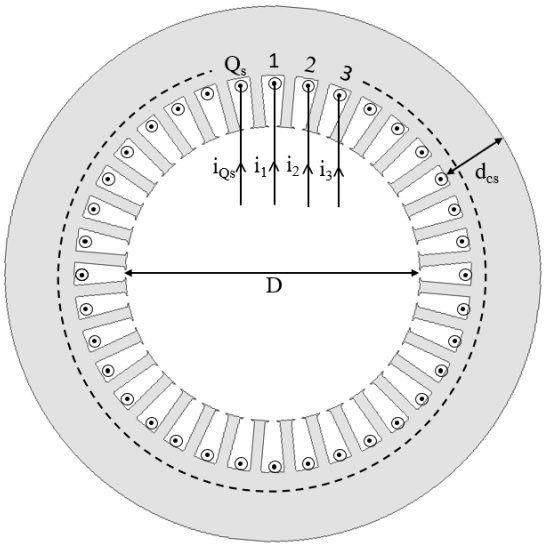

Figure 2.1: IM stator model with Q_s slots. Each slot current is explicitly captured to model different winding configurations and pole changing techniques. The core stack length is l.

2.1 Electronic Pole-Changing from a Machine Perspective

Figure 2.1 shows a stator structure with Q_s slots where each slot current is considered as an input variable i_1, i_2 ... i_{Q_s}. The stator slots represent a discretization of space with step size of $\frac{2\pi}{Q_s}$. The magnetomotive force (MMF) can be controlled at Q_s discrete points through the slot currents. The following constraint among pole count p, number of stator slots Qs, phase number n, and number of slots per pole per phase q must always hold:

$$p = \frac{Q_s}{q \times n} \tag{2.1}$$

Equation 2.1 shows that either the phase number n or the number of slots per pole per phase q, or both, must be changed to vary the stator pole count. *Pole phase modulation (PPM)* is an electronic pole-changing technique that varies the pole count by adjusting the stator excitation phase number. In PPM, q is kept constant and considered as a hardware constraint. The pole count is inversely proportional to the phase number in PPM, as seen in Eq. 2.1. This technique was introduced in [16] and has been widely adopted in the literature [14, 20, 21, 24]. The main advantage of PPM over other pole-changing methods is the utilization of higher phase numbers to create

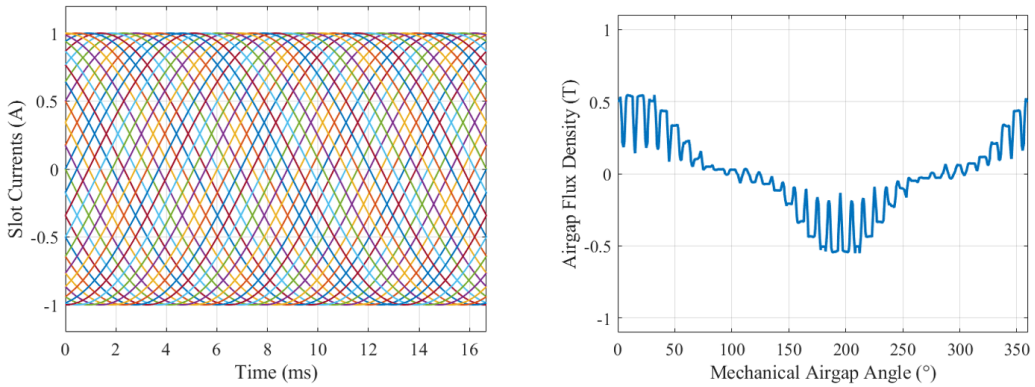

a) 36-Phase Current b) 2-Pole Flux pattern

Figure 2.2: Airgap flux density is shown in (b) as a function of the mechanical angle when the 36-phase slot current pattern shown in (a) is created. The IM is assumed to have 36 stator slots. The airgap flux density is obtained from finite element analysis (FEA).

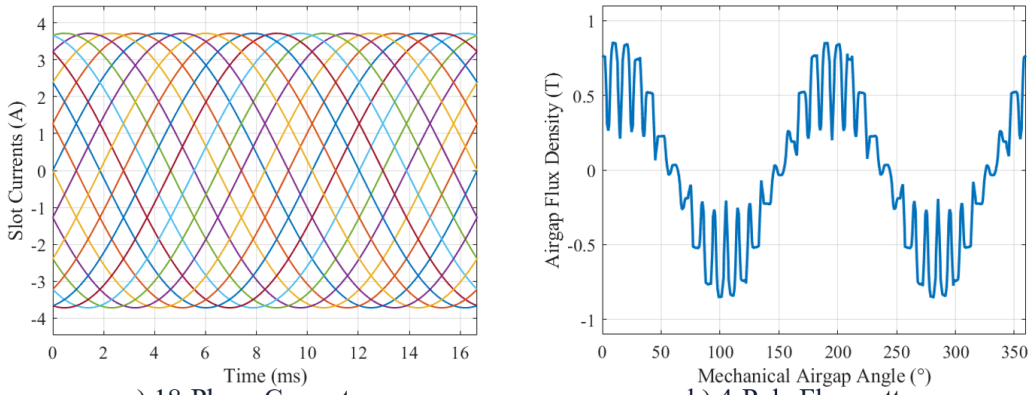

Figure 2.3: The airgap flux density is shown in (b) as a function of the mechanical angle when the 18-phase slot current pattern shown in (a) is created. When the phase number is decreased from 36 to 18, the pole count increases from two to four (compared to Fig. 2.2) as there are two identical 18-phase patterns.

near-sinusoidal airgap MMF. Higher phase numbers have a higher winding factor [29]. Using PPM, the current excitation i_j in a slot j when $q = 1$ (all slots are independently controlled) is given by

$$i_j(t,p) = \sqrt{2}Isin(\omega_e t + \frac{(j-1)\pi p}{Q_s}) \tag{2.2}$$

where I is the RMS current, and ω_e is the fundamental frequency.

Figures 2.2 and 2.3 show the airgap flux density in a 36-slot IM for different slot current patterns, as obtained from finite element analysis (FEA). This example illustrates PPM with individual control over each slot current ($q = 1$). When the phase number is decreased from 36-phase to 18-phase, the pole count increases from two to four as there are two identical 18-phase patterns. Since Figs. 2.2 and 2.3 are also showing return currents, the phase number in these figures is double the one obtained from Eq. 2.1. The phase number given in Eq. 2.1 only accounts for half of the machine slots as the excitations in the remaining slots, known as return conductors, are easy to determine due to symmetry. When the number of controllable machine terminals is smaller than Q_s, a series or parallel grouping of slots is needed. An example of series grouping of two adjacent slots is shown Fig. 2.4. The currents i_1 and i_2 are no longer independent when they are grouped in series. In this case, one of the currents, e.g. i_1, is a controllable current while the other one

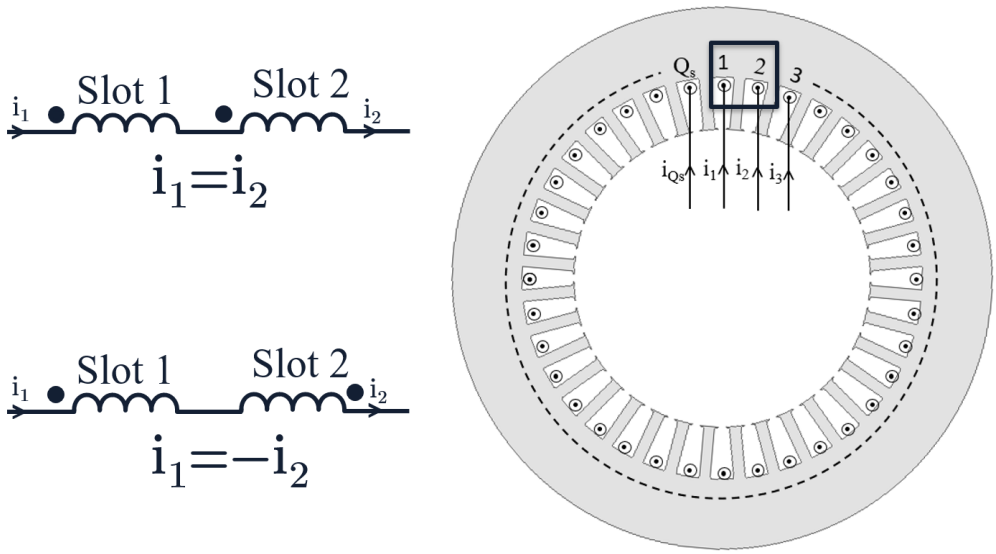

Figure 2.4: When slot conductor are grouped in series or parallel at a winding design stage, their currents are no longer independent. An example of two series grouped slot conductors is shown. The currents i_1 and i_2 must have the same magnitude but their sign depends on the physical connection.

i_2 follows it. Equation 2.2 only applies for the controllable slot currents i_1, i_3 ... i_{Q_s}. The remaining slot currents i_2, i_4 ...i_{Q_s-1} are calculated from the controllable currents. The number of controllable slot currents depends on the stator winding design.

2.2 Electronic Pole-Changing from a Power Electronics Perspective

Figure 2.5 shows a simplified schematic of the EV electric drivetrain. The power electronics converter is fed from a constrained dc bus. The number of power electronics ac ports n_{inv} must match the stator winding input terminals. From a power electronics perspective, a higher number of ac ports is needed to control more slot currents independently [26]. Thus, the stator winding and power electronics converter must be co-designed for variable-pole IM. In this section, the impact of the number of ac terminals on the pole-changing capability is investigated when PPM is used. From a power electronics perspective, the stator winding can be interpreted as a black box. The machine pole count p as a function of the inverter phase number m is

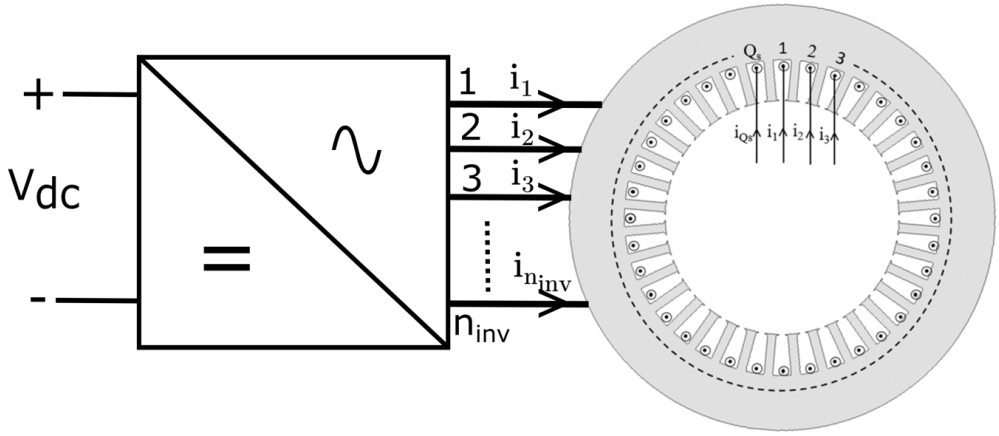

Figure 2.5: A variable-pole IM requires a high number of machine terminals driven independently by the power electronics inverter. n_{inv} is the number of ac inverter terminals which must match the number of machine stator terminals.

given by:

$$p = \frac{n_{inv}}{m} p_{min} \tag{2.3}$$

where p_{min} is the minimum pole count dependent on the stator winding design. The inverter phase number m can be different from the machine phase number n for the same pole count. This distinction is very important especially when the converter is divided into modules, which is discussed in chapter 5. For example, going back to Fig. 2.2, a 36-port inverter operates at 36-phase as seen in the current excitation while the machine phase number is 18-phase. The inverter phase number m typically ranges from 3- or 6-phase to n_{inv}-phase. The maximum pole count p_{max} is determined at the minimum phase number. At the minimum pole count p_{min}, the phase number is set to its maximum which is equal to the number of inverter legs n_{inv}. For a three-phase drive, both the minimum and maximum phase number are three which leads $p_{max} = p_{min}$. Thus, to electronically vary the pole count of a machine, more than three ac ports are required in the power electronics drive [14, 19, 26]. Although a single-phase pattern can be repeated twice in 3-phase drive, it is not desired as single-phase operation cannot rotate the magnetic field and has power ripples at double the fundamental frequency. These single-phase power ripples must be filtered through bulky capacitors in the power electronics drive [30].

CHAPTER 3

VARIABLE-POLE IM PER-SLOT MODEL

This chapter explains the effects of the IM pole count on flux and current density. A "per-slot" IM model that explicitly captures the effect of pole count on machine performance is derived next. Each slot current i_1, i_2 ... i_{Q_s} in Fig. 2.1 is explicitly modeled as input. This framework captures any n-phase/p-pole excitation without limiting the pole changing technique. The model forms the basis of the analysis done in this thesis. This chapter is adapted from [24, 25].

3.1 Effect of Pole Count on Flux Density and Current Density in a Variable-Pole IM

The value of electronic pole-changing to improve machine performance is counter-intuitive because fundamentally torque production in an IM is independent of pole count. Torque produced by an electric machine T_e is given by [31]:

$$T_e = kB_gK_sV_{rotor}\eta_{motor}cos(\phi_{gap}) \tag{3.1}$$

where K_s is the surface current density, B_g is the peak fundamental airgap flux density, V_{rotor} is the rotor volume, $cos(\phi_{gap})$ is airgap power factor, η_{motor} is the motor efficiency, and k is a constant. The rotor volume V_{rotor} can be used to get a first order approximation of the machine volume. Basically, Eq. 3.1 shows that for the same K_s and V_{rotor}, torque production is independent of pole count p, assuming the airgap flux density B_g is the same for all pole counts. For a fixed-pole IM, the machine is designed to deliver similar B_g irrespective of its pole count. However, a variable-pole IM does not require all pole counts to have the same rated torque capability, as discussed in Chapter 1.

An FEA analysis has been performed on an IM nominally designed for six

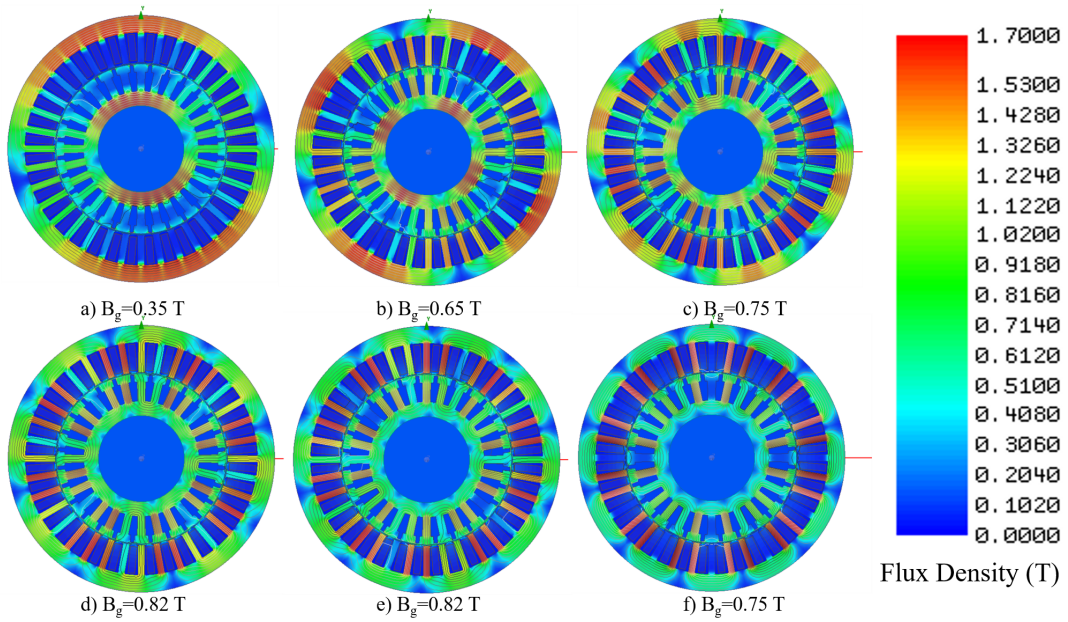

Figure 3.1: FEA simulations of a 36-slots-IM with individual slot current control. The core flux density is limited to 1.7 T for all pole counts. The flux density colormap is shown for (a) 2-pole, (b) 4-pole, (c) 6-pole, (d) 8-pole, (e) 10-pole and (f) 12-pole. B_g is the peak fundamental airgap flux density.

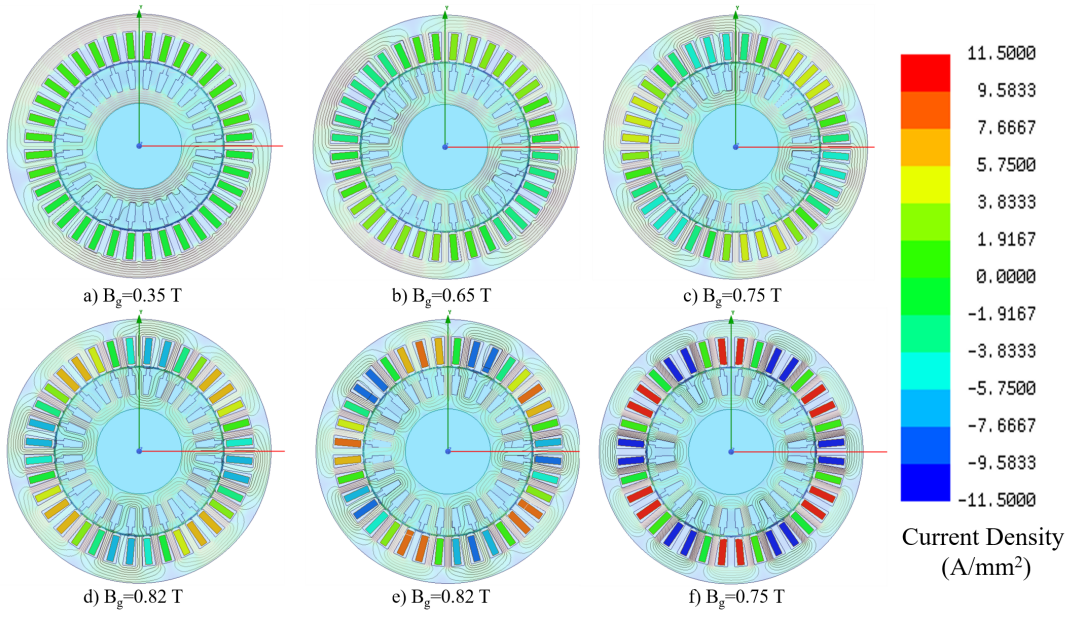

Figure 3.2: FEA simulations of a 36-slots-IM for the same conditions as Fig. 3.1. The magnetizing current density colormap is shown for (a) 2-pole, (b) 4-pole, (c) 6-pole, (d) 8-pole, (e) 10-pole and (f) 12-pole.

poles to capture the effects of pole count on electromagnetics and B_g. The machine dimensions and winding are kept the same for all pole counts. The pole count is varied by controlling the slot currents through PPM. The stator and rotor cores are made of M19-24G core material and their flux density is limited to 1.7 T to avoid deep saturation. Figures 3.1 and 3.2 show FEA flux and magnetizing current density colormaps. In Figs. 3.1-a and 3.1-b, the 2- and 4-pole configurations are constrained by stator and rotor yoke flux limits and have peak airgap flux densities of 0.35 T and 0.65 T, respectively. To extract more flux density from these lower pole counts, the stator and rotor yokes thickness can be increased [32]. However, this constrains the machine design and is not necessary for variable-pole IMs as lower pole count are used to improve high-speed torque capability and are not required to deliver the full rated torque. The yoke flux density B_y is inversely proportional to the pole count p:

$$B_y = \frac{B_g}{p}\frac{D}{k_{is}d_{cs}} \tag{3.2}$$

where D is the rotor diameter, d_{cs} is the core stator length as shown in Fig. 2.1, and k_{is} is the ratio of the effective motor axial length to its actual axial length [31]. The same equation can be derived for the rotor yoke flux density by replacing d_{cs} with the rotor yoke length. As seen in Fig. 3.1 and Eq. 3.2, the yoke flux density decreases as the pole count increases for the same airgap flux density B_g. The peak airgap flux density B_g increases with pole count until 8-pole, as seen in Figs. 3.1 (a-d). With higher airgap flux density, higher torque can be extracted from the machine with the same rotor bar current. Alternatively, lower rotor bar current can be used to produce the same torque with a higher airgap flux density. Beyond eight poles, Figs. 3.1-e and 3.1-f show that tooth flux density constrains the peak airgap flux density although the yoke is well below saturation. The tooth flux density is directly proportional to the airgap flux density and is independent of the pole count p.

While Fig. 3.1 suggests that higher pole counts are better as they allow higher airgap flux density, the magnetizing current must also be taken into consideration to understand the complete trade-off between magnetic flux density and the current density. Figure 3.2 shows that higher pole counts trade off their higher airgap flux density for a higher no-load (magnetizing) current. Even for the same airgap flux density, higher pole counts require

more magnetizing current as seen by comparing 8- and 10-pole in Figs. 3.1 and 3.2. Assuming the core is not saturated, the peak magnetizing current I_m as a function of p and B_g is

$$I_m(B_g, p) = \frac{\pi g B_g}{\mu_0 Q_s N k_w} p \tag{3.3}$$

where g is the airgap length, μ_0 is the free space permeability, N is the number of turns in each slot, and k_w is the winding factor. As seen in Eq. 3.3, a higher magnetizing is required for the same airgap flux density with a higher pole count. Lower pole counts produce their flux more effectively with smaller no-load magnetizing current. A lower magnetizing current yields a better power factor and smaller no-load losses. At light loads where a partial flux density is needed, lower pole counts have a major advantage of smaller magnetizing current and losses.

In summary, Figs 3.1 and 3.2 showed the tradeoffs between magnetizing current and flux densities in variable-pole IMs. No single pole configuration is best in terms of both magnetic and no-load current density. These insights are used in the following chapters to derive techniques to select the pole count in applications with broad operating regime like EVs.

3.2 Per-Slot Model of Variable-Pole IM

The "per-slot" steady-state model is derived in this section. Pole count p is modeled as an explicit variable. A multi-phase excitation can be transformed to a stationary reference frame of $\alpha - \beta$ components [29]. In the per-slot model, the Clarke matrix transforms each of the Q_s slot variables to $\alpha - \beta$ subspaces, where each pole count p is associated with its own subspace. The remaining subspaces are the zero-sequence components. For example, the transformation matrix of a Q_s-slot IM when each slot is individually

controlled using PPM (q=1) is

$$K(p,n,Q_s) = \begin{bmatrix} 1 & cos\delta & cos2\delta & ... & cos(Q_s-1)\delta \\ 0 & sin\delta & sin2\delta & ... & sin(Q_s-1)\delta \\ 1 & cos2\delta & cos4\delta & ... & cos(Q_s-1)2\delta \\ 0 & sin2\delta & sin4\delta & ... & sin(Q_s-1)2\delta \\ 1 & cos3\delta & cos6\delta & ... & cos(Q_s-1)3\delta \\ 0 & sin3\delta & sin6\delta & ... & sin(Q_s-1)3\delta \\ ... & ... & ... & ... & ... \\ 1 & 1 & 1 & ... & 1 \end{bmatrix} \tag{3.4}$$

where δ is given by

$$\delta = \frac{2\pi}{Q_s} \tag{3.5}$$

The first 2 rows of matrix (3.4) correspond to 2-pole $\alpha - \beta$ components. Rows 3 and 4 where δ is replaced by 2δ correspond to 4-pole. Rows 5 and 6 where δ is replaced by 3δ correspond to 6-pole. The matrix $K(p,n,Q_s)$ is orthogonal. This implies that the subspaces of different pole counts are orthogonal to each other. Physically, this means that a 2-pole current excitation creates a 2-pole pattern only and does not affect the 4-pole subspace. Since the transformation models each slot explicitly, any $n-$phase/$p-$pole configuration is captured in this framework. The transformation is used to generate voltage, current and flux $\alpha - \beta$ components. A standard $\alpha - \beta$ to $d-q$ transformation is used to rotate the stationary coordinates to the rotor flux reference frame [33]. The rotation operation preserves the vector amplitude. Once in a $d-q$ reference frame, any well-established $d-q$ model of an IM can be used for further analysis, while explicitly outlining the impact of pole count on the parameters and variables. The standard steady-state $d-q$ model in the rotor-flux reference frame of an IM [33] is rewritten here to match the notation and definitions of the per-slot model:

$$v_{ds} = R_s i_{ds} - \omega_e \lambda_{qs} \tag{3.6}$$

$$v_{qs} = R_s i_{qs} + \omega_e \lambda_{ds} \tag{3.7}$$

$$0 = R'_r i'_{dr} \tag{3.8}$$

$$0 = R'_r i'_{qr} + \omega_s \lambda'_{dr} \tag{3.9}$$

$$\lambda_{ds} = L_s i_{ds} \tag{3.10}$$

$$\lambda_{qs} = L_s i_{qs} + L_m i'_{qr} \tag{3.11}$$

$$\lambda'_{dr} = L_m i_{ds} \tag{3.12}$$

$$\lambda_{qr} = L_m i_{qs} + L'_r i'_{qr} \tag{3.13}$$

$$\omega_e = \frac{p}{2}\omega_m + \omega_s \tag{3.14}$$

Here, rotor parameters and variables are referred to the stator. For example, L'_r and R'_r are the rotor self-inductance and resistance referred to each stator slot, respectively. i'_{dr} and i'_{qr} are rotor d-axis and q-axis currents referred to the stator, respectively. ω_s is the slip frequency in electrical rad/s. λ_{ds} and λ_{qs} are stator d- and q-axis flux linkages, respectively. λ'_{dr} is the rotor flux linkage referred to the stator. ω_m is the rotor speed in mechanical rad/s. i_{ds} and i_{qs} are the stator d- and q-axis currents, respectively. v_{ds} and v_{qs} are the stator d- and q-axis voltages, respectively. L_m is the magnetizing inductance of each stator slot. L_s is the self-inductance of a stator slot, which includes leakage and magnetizing components, and R_s is the stator slot resistance. The equivalent magnetizing inductance L_m in the "per-slot" model relates the airgap flux linkage with the magnetizing current of a single slot and depends on the pole count p

$$L_m = \frac{Q_s}{p^2} C \tag{3.15}$$

where C is given by:

$$C = \frac{\mu_0 D l N^2 k_w^2}{\pi g} \tag{3.16}$$

where l is machine stack length, shown in Fig. 2.1. The magnetizing inductance L_m is inversely proportional to the square of pole count, which implies that the magnetizing current increases with pole count as was shown in Eq. 3.3. The amplitude of $d-q$ vectors is related to the slot quantities by:

$$X_{ds}^2 + X_{qs}^2 = (\frac{Q_s}{2} X_1)^2 \tag{3.17}$$

where X_1 can be the peak slot voltage, current or flux linkage. Finally, the machine torque is given by:

$$T_e = \frac{1}{p}\frac{C}{1+\sigma_r} i_{ds} i_{qs} \tag{3.18}$$

where σ_r models the rotor leakage [33]. The ratio $\frac{i_{ds}}{p}$ is roughly proportional to the airgap flux density. i_{qs} is roughly proportional to the rotor bar current. Equation 3.1 can be derived from Eq. 3.18 by ignoring the leakage term. The stator and rotor copper losses in the per-slot $d-q$ model are given by:

$$P_{s,copper} = \frac{2}{Q_s} R_s (i_{ds}^2 + i_{qs}^2) \tag{3.19}$$

$$P_{r,copper} = \frac{2}{Q_s} R_r' \frac{i_{qs}^2}{(1+\sigma_r)^2} \tag{3.20}$$

where $P_{s,copper}$ and $P_{r,copper}$ are the total stator and rotor copper losses. Core losses P_{core} are estimated using the Steinmetz equation [34]:

$$P_{core} = C_h f B^{\gamma} + C_e f^2 B^2 \tag{3.21}$$

where B is the peak flux density, γ in an empirical constant, f is the fundamental frequency in Hz, and C_h and C_e are hysteresis and Eddy current constants extracted from the core material datasheet, respectively.

3.3 Approximate Variable-Pole IM model

In this section, the per-slot model is simplified to an approximate model. Although the approximate model is less accurate, its simplicity is useful to get insights on the effect of pole count on stator current and machine losses. Stator resistance R_s and stator and rotor leakages are ignored. Following these assumptions, λ_{ds} and i_{ds} simplify to

$$\lambda_{ds} = \frac{Q_s}{2}\frac{V}{\omega_e} \tag{3.22}$$

$$i_{ds} = \frac{V}{\omega_e}\frac{1}{2C} p^2 \tag{3.23}$$

where V is the per-slot peak voltage. The d-axis current is the same as the magnetizing current. As shown in section 3.1, the magnetizing current increases with the pole count p. For a given $\frac{V}{\omega_e}$ ratio, magnetizing current i_{ds} is proportional to p^2. With the same $\frac{V}{\omega_e}$, magnetizing current is reduced by a factor of nine when the pole count is changed from 6- to 2-pole. Thus, lower pole counts cut down magnetizing current significantly. The approximate q-axis current i_{qs} is given by

$$i_{qs} = \sqrt{\left(\frac{Q_s}{2}I\right)^2 - \left(\frac{V}{\omega_e}\frac{1}{2C}p^2\right)^2} \tag{3.24}$$

where I is the peak slot current. Replacing the approximate currents i_{ds} and i_{qs} in Eq. 3.18 and setting σ_r to zero, the approximate torque equation is given by

$$T_e = \frac{V}{2\omega_e}p\sqrt{\left(\frac{Q_s}{2}I\right)^2 - \left(\frac{V}{\omega_e}\frac{1}{2C}p^2\right)^2} \tag{3.25}$$

If we ignore the magnetizing current component in the square root term of 3.25, the torque simplifies to

$$T_e = \frac{Q_s V I}{4\omega_e}p \tag{3.26}$$

From Eq. 3.26, it can be seen that torque is proportional to the pole count p when the magnetizing current component is small enough. However, as p is increased, the magnetizing current significantly increases. The higher magnetizing current of higher pole counts limits the available headroom to inject a torque producing current component i_{qs}. Even if the machine is unsaturated, the magnetizing current can become so high with high pole counts such that it exceeds the stator current limit. In this case, torque producing current component i_{qs} can no longer be injected and switching to a higher pole count is not useful. An option to limit the magnetizing current is to reduce the stator flux by decreasing the $\frac{V}{\omega_e}$ ratio. With flux weakening, the torque capability of the IM decreases as seen in Eq. 3.25. Under flux weakened conditions, lower pole counts are much more effective in producing flux as they require a smaller magnetizing current.

CHAPTER 4

OPERATIONAL POLE SELECTION STRATEGIES

In this chapter, pole selection methods are proposed to optimize two separate characteristics, which are stator current and machine losses. In the first two sections, the approximate IM model is used to demonstrate the first order effects of pole counts on machine losses and stator current. Then, an optimization problem is formulated using the generalized per-slot model. The goal is to determine the operating region where each pole minimizes stator current and power losses. This chapter is reprinted from [24, 25].

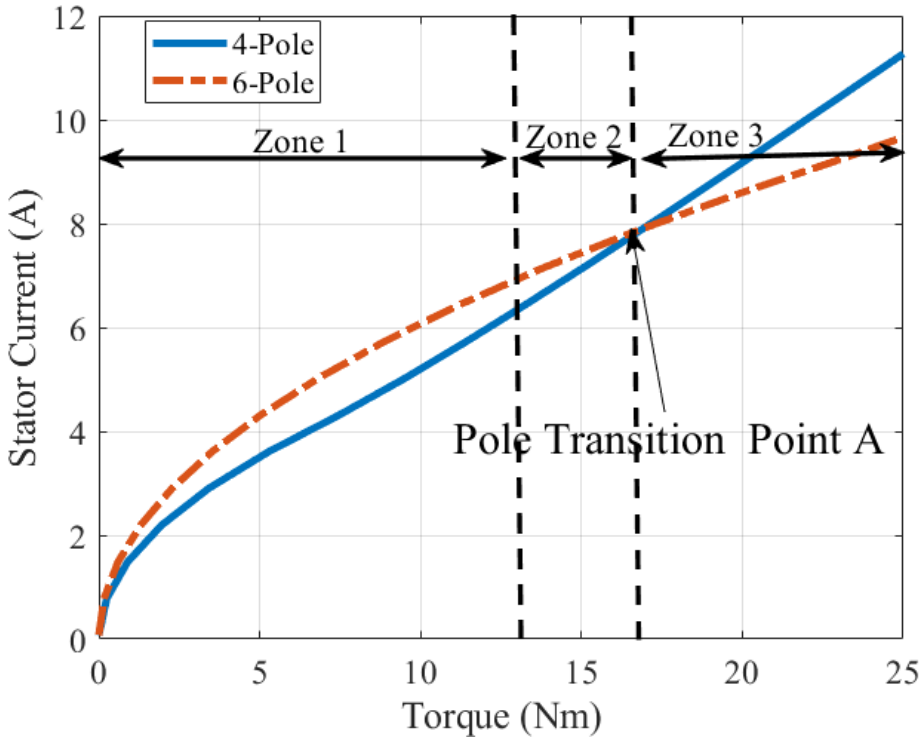

Figure 4.1: Stator current (A) versus torque (Nm) for a given IM operated with four or six poles for any speed where the inverter voltage limit is not constraining.

4.1 Maximum Torque Per Ampere (MTPA): Ideal Case

The goal of this MTPA strategy is to minimize the stator current required to produce a given torque [35, 36]. For the ideal case, the approximate IM model is used. Equation 3.25 is used to calculate the minimum current required to produce a torque while constraining the $\frac{V}{\omega_e}$ ratio. In the ideal case, the $\frac{V}{\omega_e}$ ratio is proportional to flux linkage, as seen in Eq. 3.22. Figure 4.1 shows the required IM stator current for various torque requirements. For a torque below point A, the 4-pole configuration requires less current compared to 6-pole. Recall that the lower pole count minimizes magnetizing current and the effect of magnetizing current is dominant at light loads. Beyond point A, the 6-pole count requires less stator current as it trades off its higher magnetizing current i_{ds} for a lower q-axis current i_{qs}. At high torque, the effect of magnetizing current is small and the q-axis component i_{qs} is more

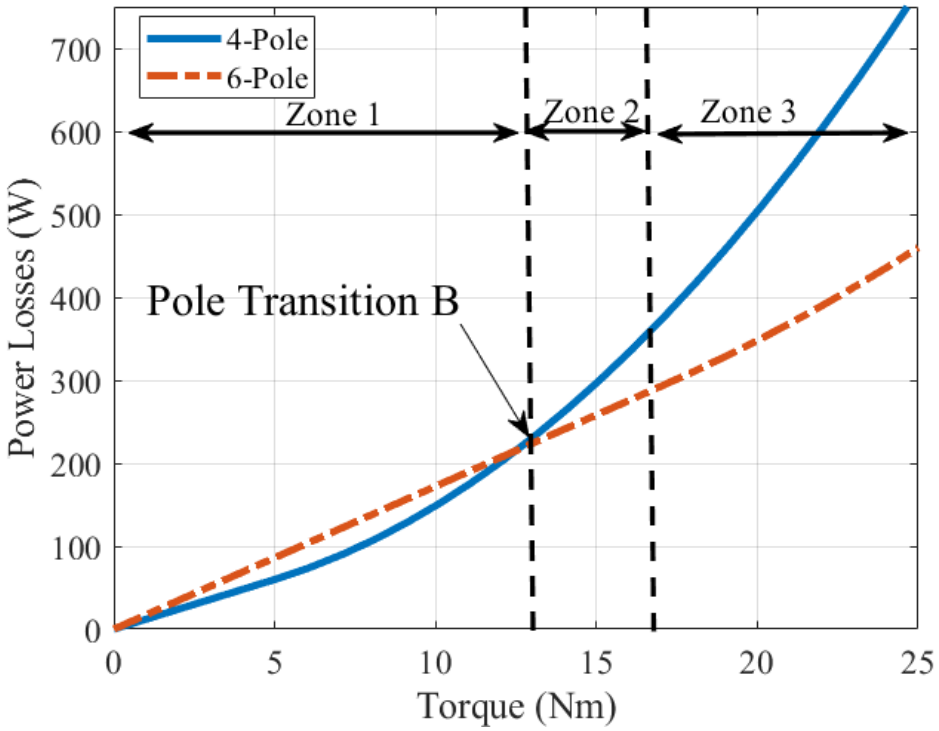

Figure 4.2: Power Losses (W) versus torque (Nm) for a given IM operated with four or six poles for any speed where the inverter voltage limit is not constraining.

dominant. The intersection point A is defined as "pole transition point" for the MTPA strategy.

4.2 Minimum Loss Operation: Ideal Case

The objective of minimum loss operation is to minimize machine losses. MTPA minimizes stator copper losses but does not necessarily minimize the overall machine losses. The objective function is the summation stator copper, rotor copper and core losses given in Eqs. 3.19-3.21. Figure 4.2 shows the machine power losses for different torque requirements. For torque below point B, a 4-pole is more efficient at producing its torque. Once torque exceeds point B, 6-pole configuration has lower losses. For low torque levels in zone 1, a low pole count minimizes magnetizing current i_{ds} and core losses as the frequency is lower for the same speed. To meet the high torque requirements in zone 3, a higher pole count trades off its higher magnetizing current for a lower i_{qs}, which tends to minimize the rotor and stator copper losses. In zone 2 of Figs. 4.1 and 4.2, MTPA and ML yield different pole count selection. Although 4-pole configuration minimizes stator current in zone 2, it is less efficient than 6-pole.

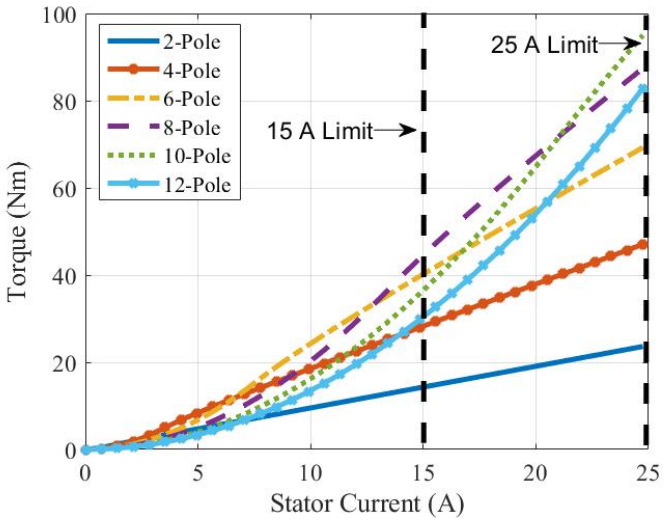

Figure 4.3: Torque capability (Nm) versus stator current (A) for pole counts from 2 to 12 poles.

4.3 Overload

Figure 4.3 shows the torque capability of pole counts from 2 to 12 as a function of stator current for the same machine. For a rated current of 15 A, the highest torque is produced by an 8-pole and there is no benefit of using higher pole counts. The 10- and 12-pole configurations are limited by tooth saturation and require a huge magnetizing current, as seen in Figs. 3.1 and 3.2. If pushing short transient overload of 25 A is allowed, 10-pole configuration produces the highest torque. Thus, pole-changing can improve overload capability.

4.4 Non-Ideal Case: Optimization Problem Formulation

In this section, an optimization problem is formulated to select the pole count that minimizes an objective function for a given torque T_e at a mechanical speed ω_m. The objective function depends on the strategy and is expressed in terms of the i_{ds} and i_{qs}. For example, the MTPA objective function is

$$f(i_{ds}, i_{qs}) = i_{ds}^2 + i_{qs}^2 \tag{4.1}$$

The model of section 3.2 is used to derive the constraints. The equality constraints ensure that the machine is delivering the required torque T_e, at a speed of ω_m. The inequality constraints ensure that the current, voltage and flux limits are not violated. The decision variables are the pole count p and currents i_{ds} and i_{qs}:

$$x = \begin{bmatrix} p & i_{ds} & i_{qs} \end{bmatrix}^T \tag{4.2}$$

The optimal solution seeks the pole count p^* and its corresponding optimal excitation electrical excitation (i_{ds}^*, i_{qs}^*). The model of section 3.2 is used to obtain the constraints and express in terms of the decision variables. The optimization problem is formulated as

$$\min_x f(x)$$

subject to:

1. Equality constraint linking the mechanical speed ω_m to the slip and electrical frequencies

$$\omega_e - \frac{p}{2}\omega_m - \frac{R'_r}{L'_r}\frac{i_{qs}}{i_{ds}} = 0 \tag{4.3}$$

2. Equality constraint that ensures the required torque T_e is delivered

$$T_e - \frac{1}{p}\frac{C}{1+\sigma_r} i_{ds} i_{qs} = 0 \tag{4.4}$$

3. Inequality constraint that limits the machine and drive currents

$$i_{ds}^2 + i_{qs}^2 \leq (\frac{Q_s}{2}\hat{I}_{rated})^2 \tag{4.5}$$

4. Inequality constraint limiting the machine voltage to its rated value set by the dc bus and PWM strategy

$$(R_s i_{ds} - \omega_e k L_s i_{qs})^2 + (R_s i_{qs} + \omega_e L_s i_{ds})^2 \leq (\frac{Q_s}{2}\hat{V}_{rated})^2 \tag{4.6}$$

5. Inequality flux linkage constraint to limit tooth and yoke flux densities

$$(L_s i_{ds})^2 + (k L_s i_{qs})^2 \leq (\frac{Q_s}{2}\hat{\lambda}_{rated})^2 \tag{4.7}$$

Table 4.1: Variable-Pole IM equivalent circuit parameters

Poles	**2**	**4**	**6**	**8**
R_s (Ω)	0.284	0.284	0.284	0.284
L_s (mH)	45.5	11.7	5.43	3.24
L_m (mH)	45.1	11.3	5.01	2.82
L'_r (mH)	49.9	13.7	6.62	4.03
R'_r (Ω)	0.352	0.206	0.179	0.170

Table 4.2: Variable-Pole IM current, voltage and flux limits

Quantity	**Value**
Per-Slot voltage limit (V)	20
Per-Slot current limit (A)	20
Flux-linkage limit (Wb-t)	0.08

where $\hat{I}_{rated}$, $\hat{V}_{rated}$ and $\hat{\lambda}_{rated}$ are the peak rated slot current, voltage and flux linkage, respectively. k is a constant that reflects stator and rotor leakage. Flux linkage constraint can be adjusted to reflect partial saturation [37]. Machine parameters depend on the pole count p. For example, the magnetizing inductance L_m varies with the square of the pole count, as seen in Eq. 3.15. Rotor parameters vary with pole count since the end-ring currents depend on pole count [31]. Stator resistance does not depend on pole count. Different pole counts may operate at different points on the B-H curve and this may change the leakage, especially once the core is pushed closer to saturation.

4.5 Case Study: Results and Discussion

Consider the IM with the per-slot parameters given in Tables 4.1 and 4.2. The optimization problem is solved over a wide range of torque and speed points to provide a map of pole count choices. Figures 4.4 and 4.5 show the optimal pole colormap for MTPA and minimum loss operation, respectively. For both

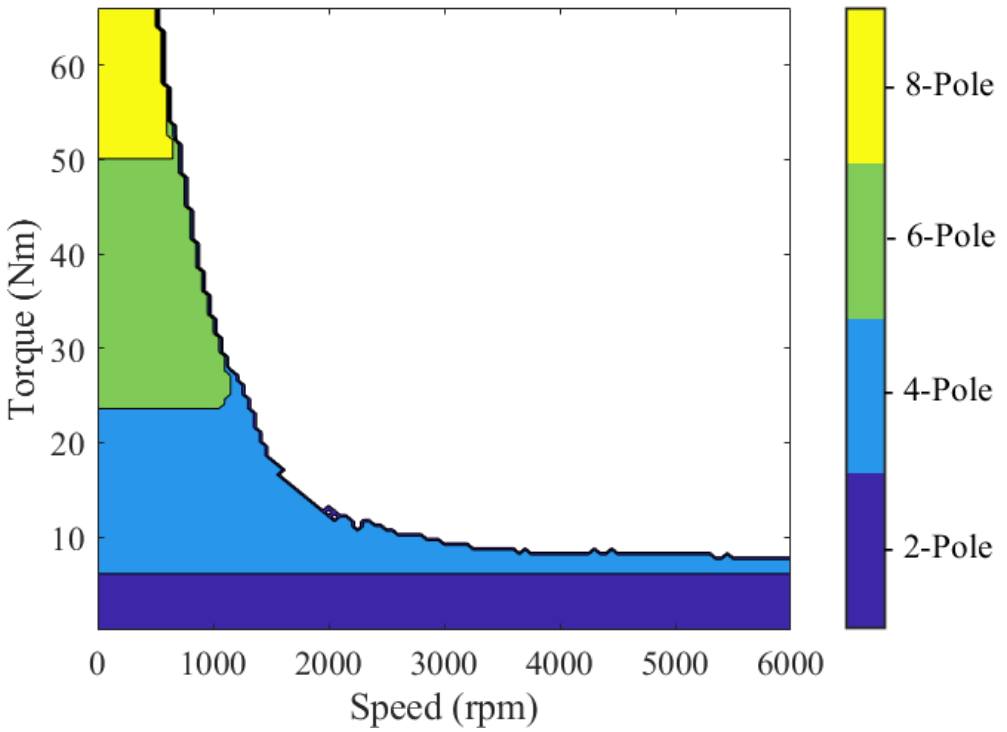

Figure 4.4: Optimal pole colormap based on MTPA.

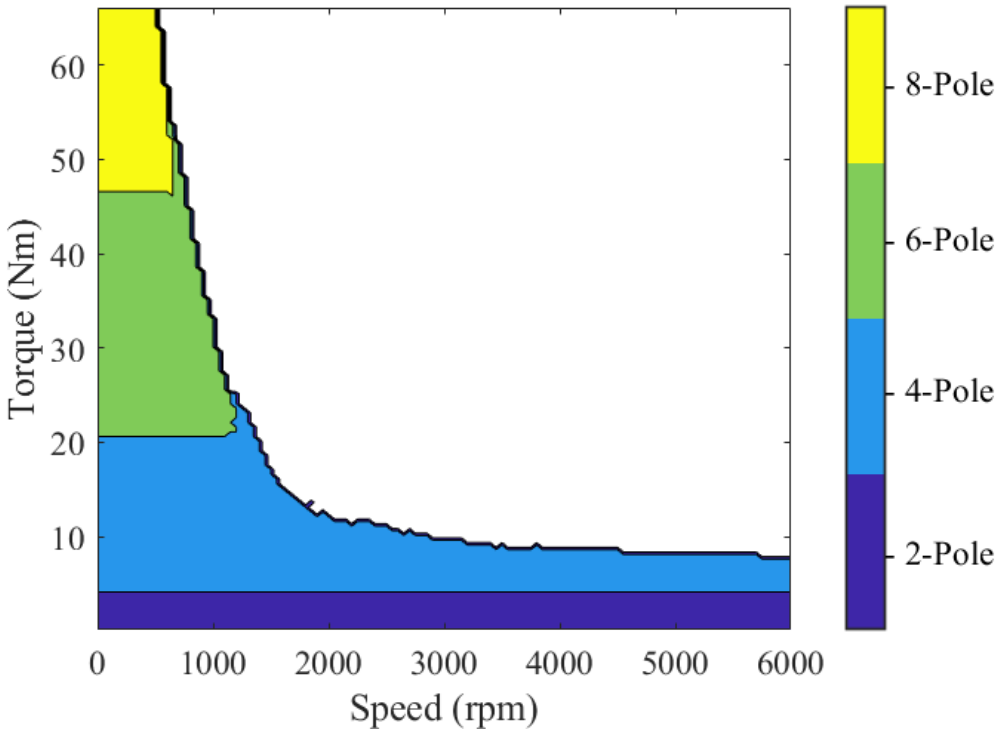

Figure 4.5: Optimal pole colormap based on minimum loss operation.

strategies, the optimal pole count is gradually shifted from 2- to 4- to 6- to 8-poles as the torque increases from zero to full value. As expected from the insights built using the approximate model, lower pole counts are the choice to produce partial torques as they require a smaller magnetizing current i_{ds}. Each pole count loses torque capability and becomes less attractive above its base speed. Higher pole counts have a lower base speed because they operate at a higher frequency for the same mechanical speed and are more constrained by the dc bus voltage V_{dc}. Beyond base speed, the inverter ac voltage is held constant which leads to a decrease in magnetizing current i_{ds} and airgap flux density B_g. The decrease in i_{ds} must be made up for by an increase in i_{qs}. Thus, in flux weakening, higher pole counts lose their main advantage, which is a reduced i_{qs}. This is why higher pole counts are not attractive at high speeds. Moreover, the effect of the leakage inductance becomes dominant at high speeds. A shift to lower pole counts is inevitable as the machine speed increases. Both strategies have similar colormaps with different boundary regions for each pole count.

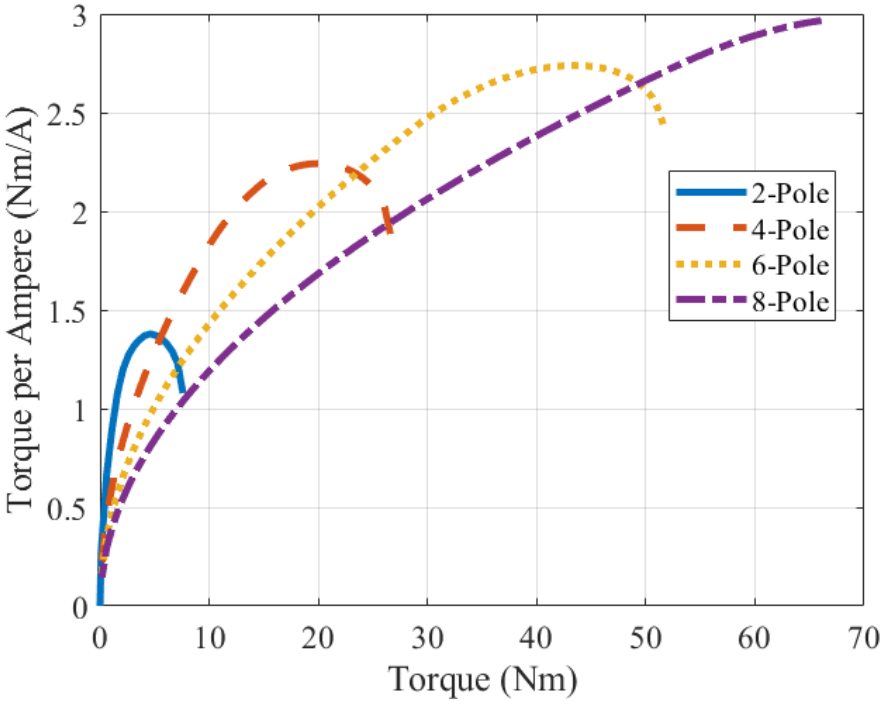

(a)

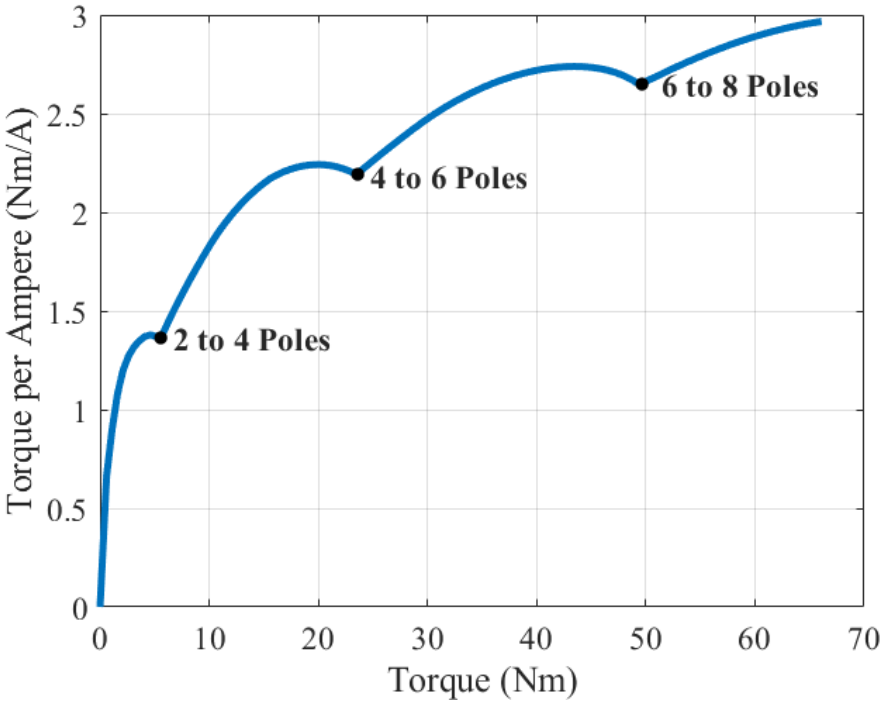

(b)

Figure 4.6: Optimal pole count at stall: torque-per-ampere for MTPA control shown for (a) each individual pole count (b) variable-pole operation.

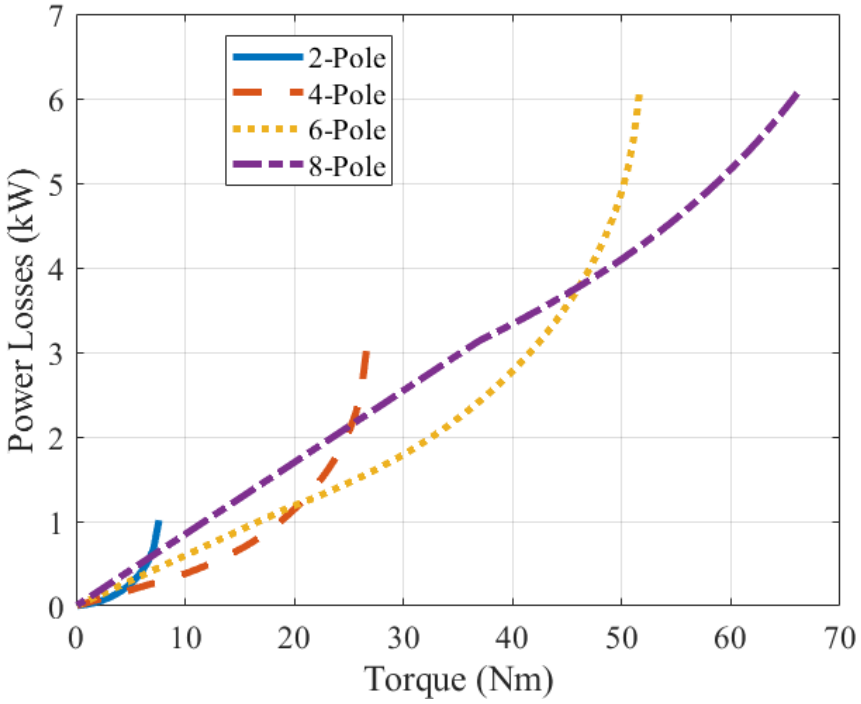

(a)

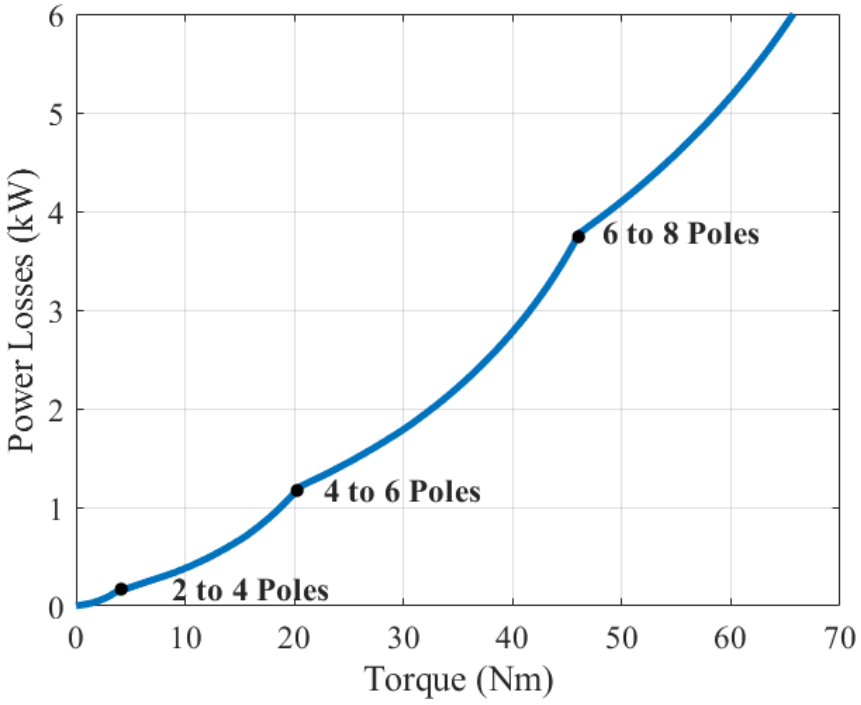

(b)

Figure 4.7: Optimal pole count at stall: power loss for minimum loss operation shown for (a) each individual pole count (b) variable-pole operation.

Figures 4.6 - 4.7 show the torque-per-ampere and machine power loss plots under stall conditions. Pole transition points are indicated in Figs. 4.6-b and 4.7-b. Pole counts with lowest power losses and highest torque-per-ampere are chosen. Optimal pole colormaps are built by doing the same analysis shown in Figs. 4.6 - 4.7 over the entire speed range. It can be seen in Fig. 4.7 that the torque-per-ampere saturates at high torque values. This suggests that increasing the pole count indefinitely is not very useful because of high magnetizing current and tooth saturation. The torque-per-ampere of each pole configuration has an optimum point beyond which it starts dropping, as seen in Fig. 4.6. The torque capability of each pole count is limited after optimum point. Although the small i_{ds} of lower pole counts can be made up for by a higher i_{qs} in the ideal analysis, this does not apply when leakage inductance is considered as it constrains machine breakdown torque. Figure 4.8 shows the torque-per-ampere and power losses at a speed of 1500 rpm. At this speed, 6- and 8-pole configurations are flux weakened and lose their advantage as their magnetizing current drops. Thus, these higher pole counts must make up their decreased flux with an increased rotor bar current. At 1500 rpm, 6- and 8-pole do not minimize losses or maximize torque-per-ampere for any torque. Thus, lower pole counts are the choice to produce partial torques and cruise at high speeds. Higher pole counts are only used if a high torque is required at low speeds.

Figure 4.9 shows i_{ds} and i_{qs} at stall for variable-pole operation. At each pole transition point, a tradeoff between i_{ds} and i_{qs} is observed. Ideally, unconstrained MTPA sets $i_{ds} = i_{qs}$. Eventually, each pole count becomes flux constrained (i_{ds} cannot be increased further) and the increase in torque is obtained through i_{qs}. Each pole transition point brings back the operation to an ideal MTPA solution ($i_{ds} = i_{qs}$) for a certain range. The minimum loss strategy uses different current values compared to MTPA for most operating points, because MTPA and ML have different objectives.

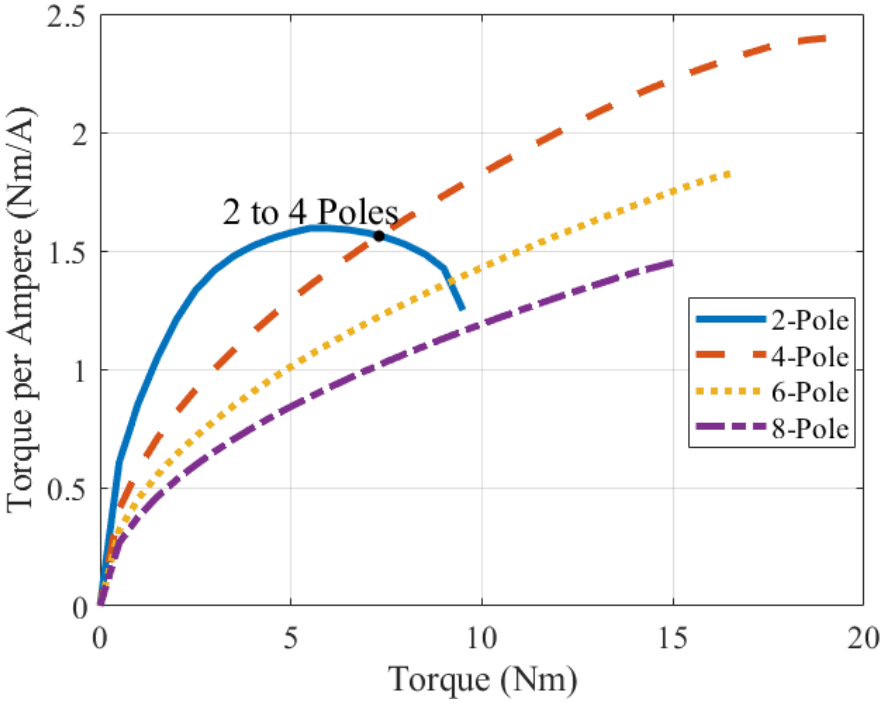

(a)

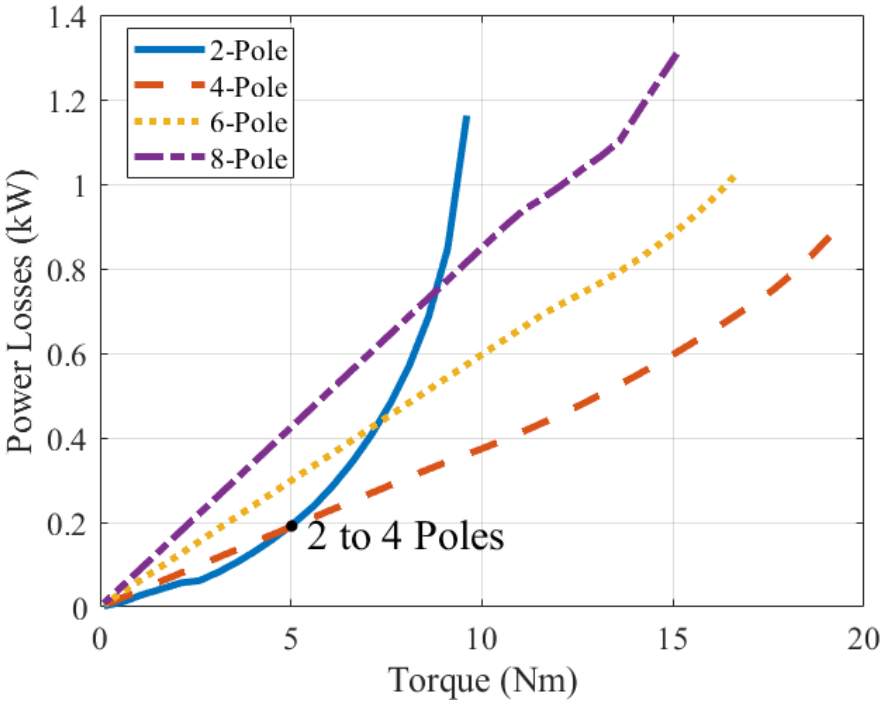

(b)

Figure 4.8: Optimal pole count at a speed of 1500 rpm for (a) MTPA and (b) minimum loss operation. Both 6- and 8-pole are flux weakened and they do not minimize losses and stator current in any operating region at this speed.

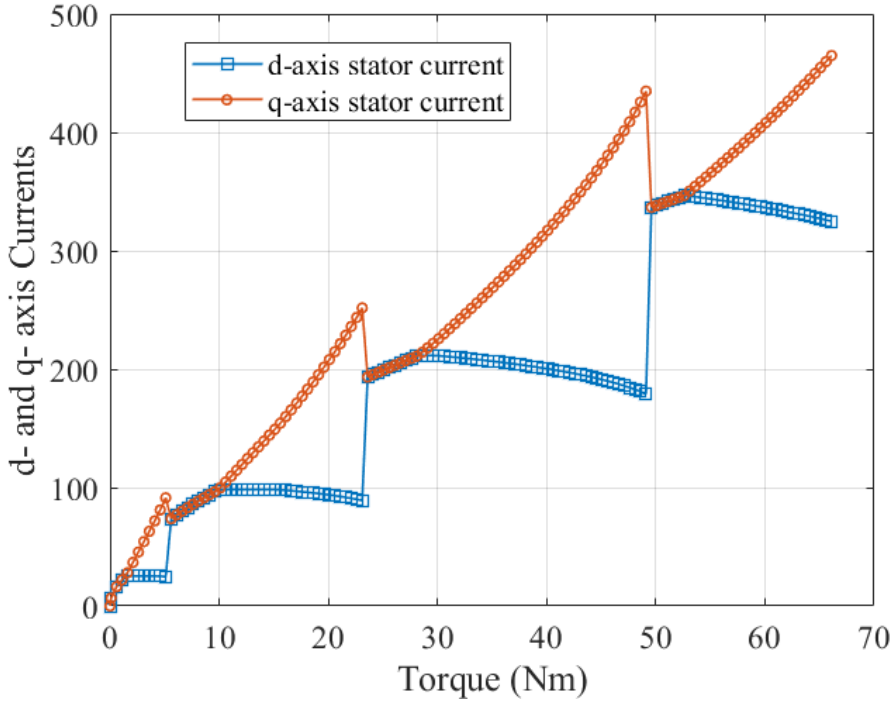

(a)

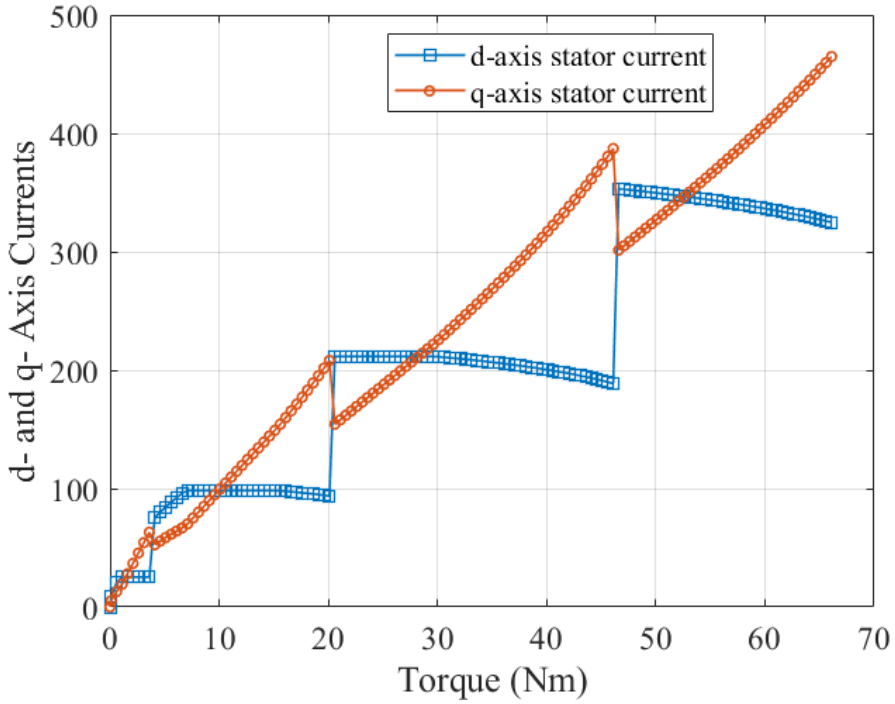

(b)

Figure 4.9: d-axis and q-axis currents i_{ds} and i_{qs} at stall for (a) MTPA and (b) minimum loss strategies.

CHAPTER 5

POWER ELECTRONICS CONVERTER DESIGN

The benefits of pole-changing from a machine perspective were shown in the previous chapter. This chapter investigates the design of power electronics drives for pole-changing IMs. An inverter with high number of ac ports n_{inv} is required to vary the IM pole count. Inverters with three or more ac terminals are known as multiphase drives. Multiphase drives can be divided into modules whose dc sides are series stacked or parallel stacked [38, 39], as shown in Fig. 5.1. The number of modules with series stacked dc sides is defined as n_s while the number of modules with parallel stacked dc sides is defined as n_p. The first section highlights the constraints imposed by pole-changing on inverter modularization. Then, the effect of the number of ac

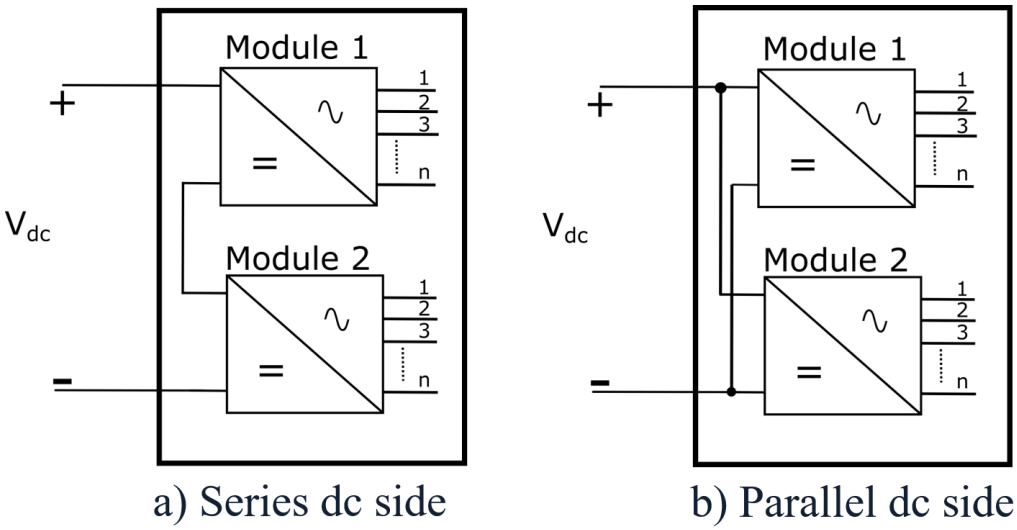

Figure 5.1: Multiphase drives can be divided into modules with their dc sides connected in (a) series or (b) parallel. n_s is the number of modules with series stacked dc sides while n_p is the number of parallel stacked dc sides. In this figure, (a) is an example of $n_s = 2$ while (b) corresponds to $n_p = 2$.

terminals on efficiency and capacitor sizing is investigated. This chapter has been accepted for publication in [26].

5.1 Modular Multiphase Drives and Pole-Changing

In Chapter 2, the relation between inverter phase number m and pole count p was given in Eq. 2.3. For the case where $n_s = n_p = 1$ (no modularization), Eq. 2.3 is still valid. However, when $n_s \neq 1$ or $n_p \neq 1$, Eq. 2.3 is extended to determine the phase number of each individual inverter module m_{mod}

$$m_{mod} = \frac{n_{inv}}{n_s n_p} \frac{p_{min}}{p} \tag{5.1}$$

When there is no modularization $n_s = n_p = 1$, Eq. 5.1 is identical to Eq. 2.3. Module phase number m_{mod} is smaller than overall inverter phase number m which can be problematic. Lower bound on inverter phase number

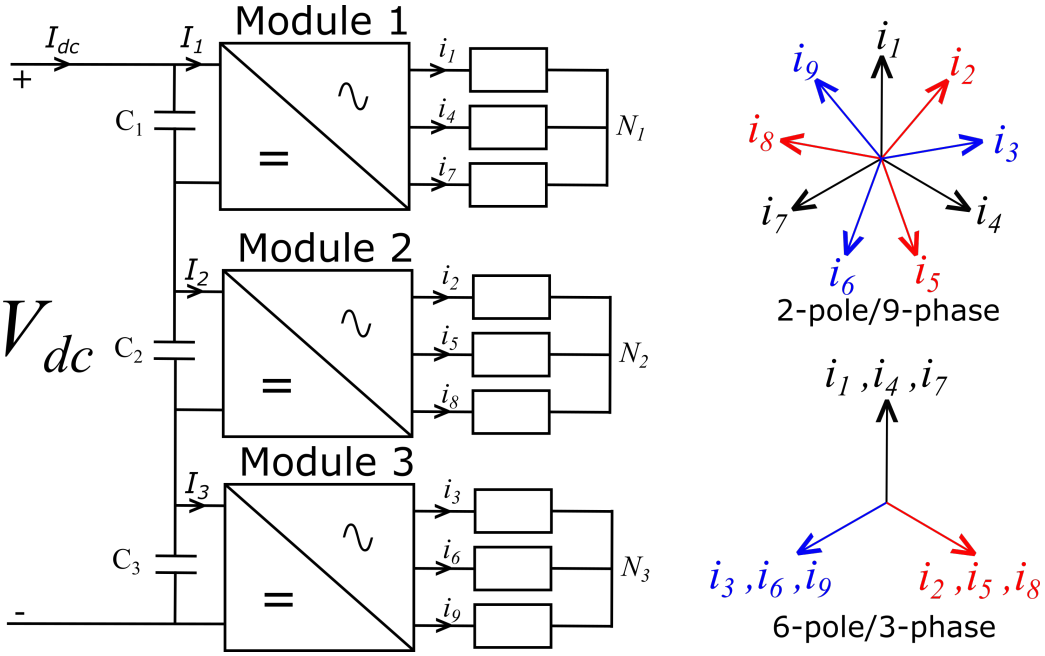

Figure 5.2: 9-leg inverter divide into $n_s = 3$ modules. At 2-pole, the inverter phase number is $m = 9$ while the phase number in each 3-leg module is $m_{mod} = 3$. At 6-pole, the inverter phase number is $m = 3$ while the phase number in each 3-leg module is $m_{mod} = 1$. Each inverter module operates as single-phase at 6-pole. Thus, 6-pole operation is not possible in this inverter configuration.

m is 3-phase to create a rotating magnetic field in the machine and avoid pulsating power. However, since inverter module phase m_{mod} is smaller than m, single phase operation can result in modules. Single-phase operation is undesired in power electronics modules as it requires bulky energy storage, complicates control and requires a full-bridge topology. Figure 5.2 shows a 9-leg inverter divided into three series stacked modules $n_s = 3$. Current vectors corresponding to the same 3-leg module have the same color. At 2-pole, the overall inverter is creating a 9-phase pattern $m = 9$ while each individual 3-leg module is seeing a 3-phase excitation $m_{mod} = 3$. At 6-pole, the net excitation is a 3-phase $m = 3$. However, each inverter module must be operated as a single-phase $m_{mod} = 1$, as seen in Fig. 5.2. The currents in each module do not sum to zero which violates the fundamentals of the Y connection. Thus, 6-pole configuration is not possible. One possible solution is to use full bridge converters. However, power ripples at double the fundamental frequency will exist in each module and buffering this power ripple is challenging [26]. Dividing inverter into modules can limit the flexibility of pole-changing if each inverter module is not operating as a multiphase converter at all pole counts. Phase numbers $m_{mod} = 1$ and $m_{mod} = 2$ must be avoided for all pole counts p.

5.2 Switch VA Rating in Modular Multiphase Drives

The breakdown voltage rating V_{rating}, current rating I_{rating}, and voltampere rating VA_{rating} of a single switch in the modular multiphase drive of Fig. 2.5 are given by

$$V_{rating} = S_V \frac{V_{dc}}{n_s} = \sqrt{6} S_V V_{slot} C_s \tag{5.2}$$

$$I_{rating} = \sqrt{2} S_I I_{slot} C_p = \frac{2\sqrt{3} S_I S_{motor} n_s}{n_{inv} V_{dc}} \tag{5.3}$$

$$VA_{rating} = 2\sqrt{3} S_V S_I \frac{S_{motor}}{n_{inv}} \tag{5.4}$$

where C_s and C_p are the number of series and parallel connected motor slots, respectively, S_V and S_I are voltage and current safety margin factors, V_{slot} and I_{slot} are the RMS voltage and current of a single IM slot, S_{motor} is the total motor input apparent power, and the inverter is assumed to be operated

with space-vector modulation scheme. To deliver the same apparent power S_{motor} with given n_{inv} and V_{dc}, there is a tradeoff between voltage and current rating. A decrease in switch voltage rating must be compensated for by an increase its current rating and vice versa. The only way to decrease each switch VA rating is to increase the switch count, as seen in Eq. 5.4.

5.3 Switch VA Rating Effect on Switching and Conduction Losses

Figure 5.3 shows conduction loss (W) and switching energy (mJ) as a function of switch VA rating, defined as the product of its voltage and current rating. Wide bandgap devices GaN and SiC are considered. In general, conduction losses and switching energy increase with switch VA rating, as shown in Fig. 5.3. This leads to two design strategies:

- Use a low number of switching devices, with high VA rating, at the cost of high loss per device.
- Use a high number of switching devices, with low VA rating and low loss per device.

With lower number of devices, pole-changing capability is restricted. The higher flexibility to vary pole count with high number of switching devices

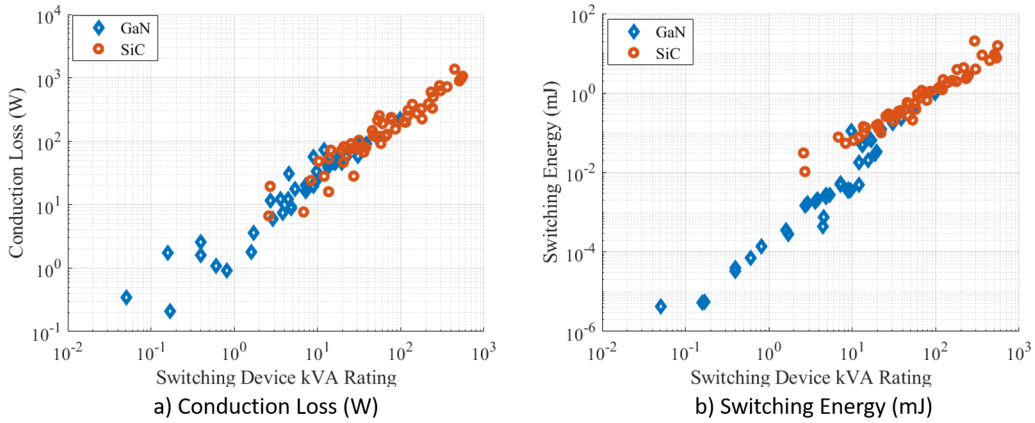

Figure 5.3: (a) Conduction losses (W) and (b) switching energy (mJ) of wide bandgap switching devices generally increase with respect to the switch kVA rating.

improves operational machine and drive efficiencies at partial loads. Lower rated devices have a larger headroom to trade off switching losses with a higher switching frequency to reduce the size of passive components. Figure 5.3 suggests that GaN devices have superior switching characteristics compared to SiC. However, GaN is currently available in lower VA rating to meet the requirement of 3-phase high power drives. With higher number of inverter ac ports n_{inv}, GaN can be deployed in high power drives to benefit from its fast switching capability.

5.4 Effect of Number of ac Ports on Inverter Losses

In this section, the effect of number of inverter ac ports n_{inv} on total drive losses is investigated. Analytical loss estimate expressions of total drive conduction P_{cond} and switching loss P_{sw} are given by:

$$P_{cond} = {C_p}^2 R_{ds} I_{slot}^2 n_{inv} = \frac{2 R_{ds} S_{motor}^2 {n_s}^2}{n_{inv} V_{dc}^2 {m_a}^2} \tag{5.5}$$

$$P_{sw} = \frac{2}{3\pi} \frac{f_{sw} S_{motor} t_{sw}}{m_a} + \frac{1}{2} \frac{f_{sw} Q_{rr} V_{dc} n_{inv}}{n_s} \tag{5.6}$$

where R_{ds} is the switch on-state resistance, m_a is the space vector modulation index, t_{sw} is the total switching time, f_{sw} is the switching frequency, and Q_{rr}

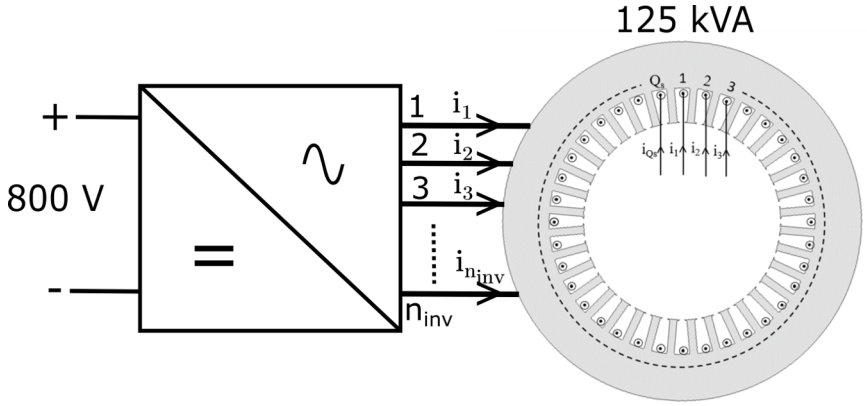

Figure 5.4: Design example: a 125 kVA motor is driven by an inverter fed from an 800 V dc bus. The inverter is switching at $f_{sw} = 50$ kHz. The number of inverter legs n_{inv} is a design variable.

is the reverse recovery charge. The parameters R_{ds}, t_{sw} and Q_{rr} are implicit functions of the device rating. The drive design example of Fig. 5.4 is considered. The goal is to determine the impact of the number of inverter ac ports n_{inv} on drive efficiency. The motor is rated for an input apparent power of $S_{motor} = 125$ kVA. The drive is fed from an 800 V dc bus and is switching at 50 kHz. The goal is to compare drives with higher number of inverter legs n_{inv} with a conventional 3-phase drive. All losses are calculated at rated condition using Eqs. 5.5-5.6 and at a junction temperature of 150 °C. As shown in Fig. 5.5, three design alternatives are considered: (a) three-phase conventional SiC-based drive, (b) 18-leg SiC-based drive $n_{inv} = 18$ and (c) 36-leg GaN-based drive divided into two series stacked modules ($n_{inv} = 36$ and $n_s = 2$). Tables 5.1 and 5.2 compare the three alternatives in terms of number of power electronic switches, kVA rating of individual switch, total conduction loss, total switching loss and total drive losses [26, 40, 41, 42]. As the switch count increases, switching loss decreases because lower VA rated devices can switch faster and handle smaller power transients. The switching loss in the 3-phase can be decreased by using a lower switching frequency at the cost of larger passives and higher harmonic distortion in the motor current. The lowest conduction loss is achieved by the 18-leg drive. Conduction loss is less sensitive than switching loss to the drive architecture. Both the 18- and 36-leg drives are much more efficient than the conventional

Table 5.1: Switch part number, switch count, voltage rating, current rating and kVA rating are indicated for the three design alternatives in Fig. 5.5 [26, 40, 41, 42].

Design	**Switch part number**	**Switch count**	V_{rating}	I_{rating}	**Switch** kVA_{rating}
(a)	SiC BSM300D12P2E001	6	1200 V	300 A	360 kVA
(b)	SiC C2M0040120D	36	1200 V	60 A	72 kVA
(c)	GaN TP65H035WSQA	72	650 V	47.2 A	30.7 kVA

Table 5.2: Total drive power losses for the three design alternatives in Fig. 5.5.

Design	**Conduction loss (W)**	**Switching loss (W)**	**Drive losses (W)**
(a)	570 W	575 W	1145 W
(b)	325 W	300 W	625 W
(c)	569 W	121 W	690 W

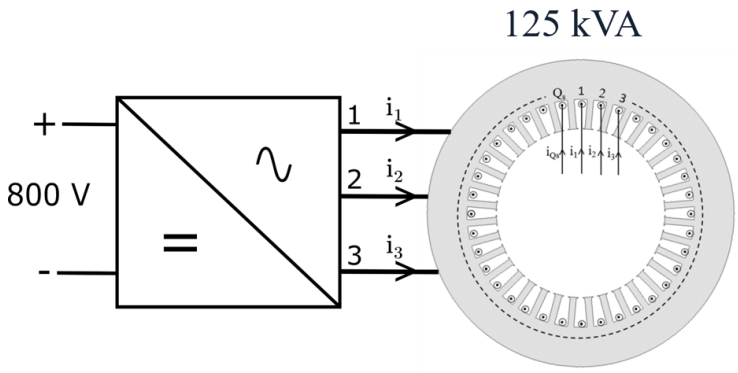

(a)

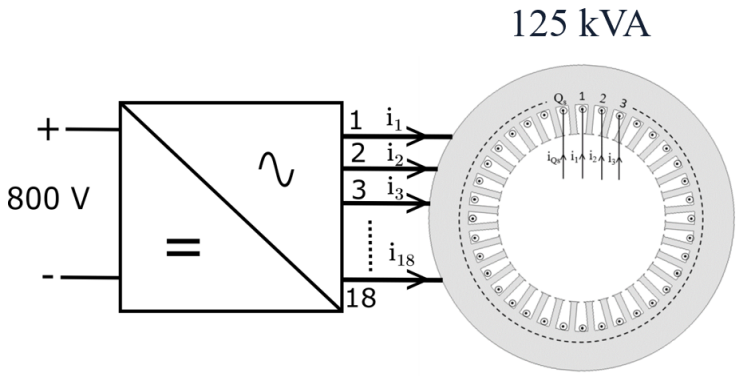

(b)

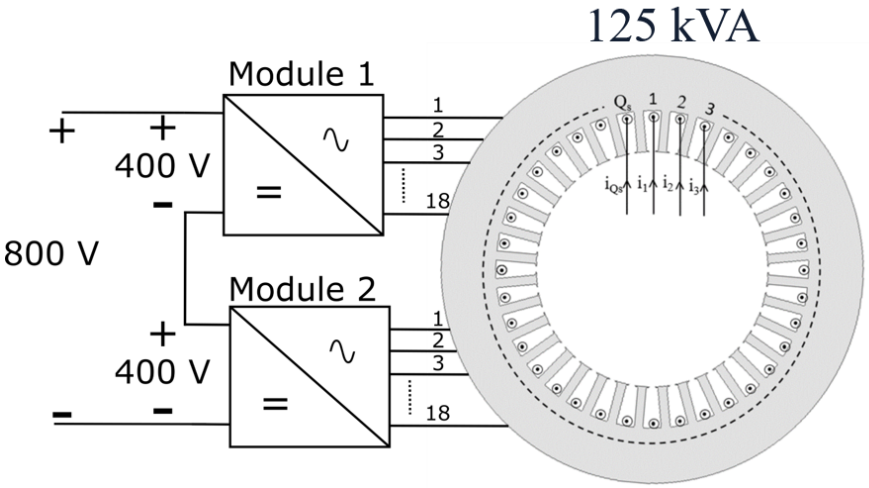

(c)

Figure 5.5: Three power electronics drive alternatives are shown. Alternative (a) is a conventional 3-phase drive. Alternative (b) is an 18-leg drive ($n_{inv} = 18$). Alternative (c) is a 36-leg drive divided into two 18-leg series stacked modules ($n_{inv} = 36$ and $n_s = 2$).

3-phase fixed-pole drive. Moreover, the 18- and 36-leg drives can vary the IM pole count to improve operational efficiency and increase machine speed range.

5.5 dc Link Capacitor Sizing for Variable-Pole IM

The dc link capacitor is an essential component of the power electronics drives as it reduces ripple current and voltage spikes caused by switching [43]. This section sizes the dc link capacitor for a modular multiphase inverter driving a variable-pole IM, assuming space-vector modulation is used. The module capacitance C for a given peak to peak dc bus voltage ripple ΔV_{pp} is

$$C = \frac{2n_s S_{motor}}{\sqrt{3} n_p f_{sw} \Delta V_{pp} V_{dc}} \max_p \hat{r}_{pp}[(m_{mod}(p)] \tag{5.7}$$

where $\hat{r}_{pp}$ is a maximum ripple term which depends on the module phase number m_{mod} [44]. For phase numbers higher than 3-phase, $\hat{r}_{pp}$ decreases and less dc bus voltage ripple is present. Beyond 6-phase, the ripple voltage only decreases marginally as phase number is increased. In variable-pole IMs, the pole count is varied by changing the phase number. Thus, the capacitor should be sized at the pole count for the worst-case voltage ripple. The maximum energy stored in all combined module capacitors E_c is given by

$$E_C = \frac{S_{motor} V_{dc} \max_p \hat{r}_{pp}[m_{mod}(p)]}{\sqrt{3} f_{sw} \Delta V_{pp}} (1 + \frac{\Delta V_{pp}}{2V_{dc}})^2 \tag{5.8}$$

Figures 5.6 and 5.7 show the energy storage (J) and power (kW) ratings of dc link capacitors for all three drive alternatives shown in Fig. 5.5. The capacitors are sized to limit the peak to peak dc bus voltage ripple to 5%. The 18- and 36-leg drives utilize higher module phase numbers m_{mod} compared to the 3-phase drive and require a smaller capacitance power and energy ratings at all pole counts except 12-pole. At 12-pole, the 18-leg and modular 36-leg drives excite a repeating pattern of 3-phase systems which significantly increases the power and energy ratings of the capacitor. The difference in capacitor sizing is marginal for pole counts which require a higher phase number than three. It is reasonable to drop 3-phase operation in drives with

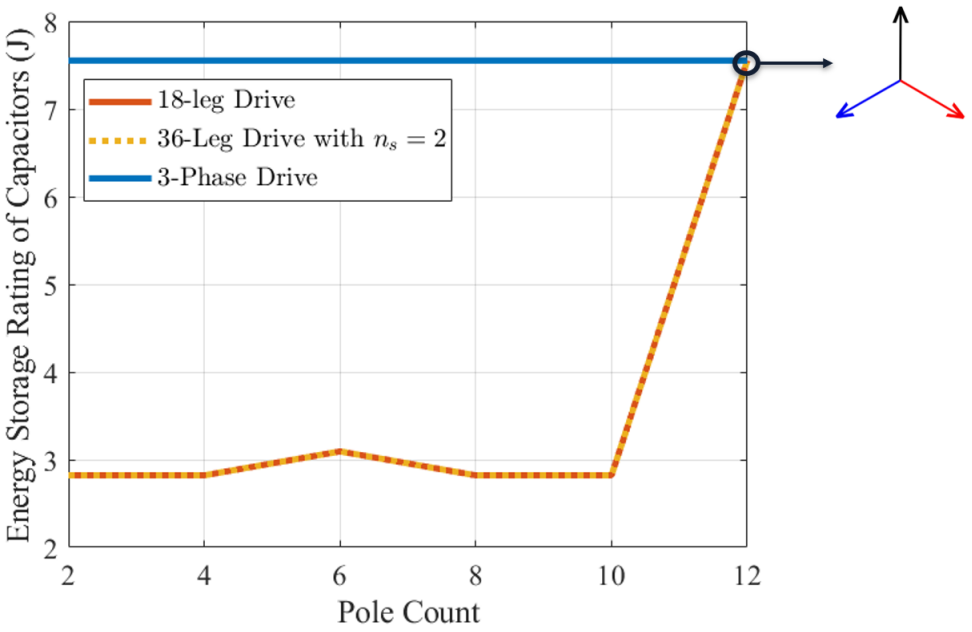

Figure 5.6: Energy storage (J) rating of all combined dc link capacitors for the 18-leg, 36-leg ($n_s = 2$) and 3-leg drives (Fig. 5.5) under the following conditions: $f_{sw} = 50$ kHz, $S_{motor} = 125$ kVA, $\Delta V_{pp} = 40$ and $V_{dc} = 800$ V.

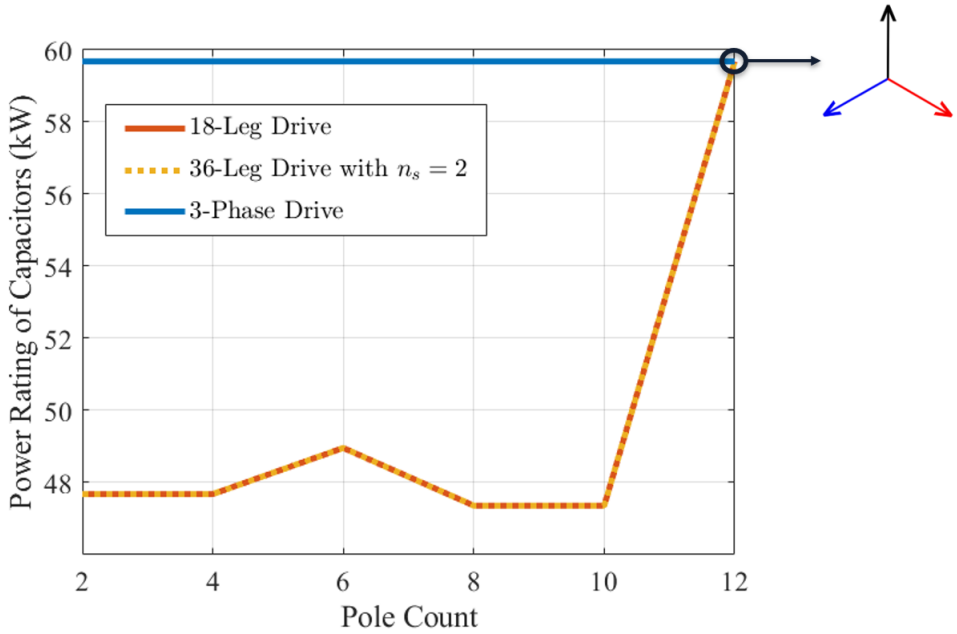

Figure 5.7: Power rating (kW) of all combined dc link capacitors for the 18-leg, 36-leg ($n_s = 2$) and 3-leg drives (Fig. 5.5) under the following conditions: $f_{sw} = 50$ kHz, $S_{motor} = 125$ kVA, $\Delta V_{pp} = 40$ and $V_{dc} = 800$ V.

high number of ac ports as 12-pole does not provide any machine benefits and constrains capacitor sizing. If 3-phase operation is avoided in drives

with high number of ac ports, dc link capacitor energy and power ratings are reduced by roughly 60% and 17%, respectively. Capacitors are bulky components of EV drives and reducing their size improves converter power density [43]. In addition, capacitor power losses are reduced when the capacitor's power rating is decreased, which further improves power conversion efficiency and simplifies capacitor cooling. The reduction of capacitor volume and increase in its temperature range are crucial to physically integrate the electric machine and its power electronics [38, 39].

CHAPTER 6

EXPERIMENTAL SETUP AND RESULTS

This chapter presents the experimental setup used to validate the theoretical analysis. Then, experimental test results for both machine and power electronics are provided and discussed. The experimental results are reprinted from [24, 25, 26].

6.1 Experimental Setup

Figure 6.1 shows the experimental 36-slot toroidally wound IM [14]. The prototype has 72 terminals which allows us to externally access each slot conductor, as shown in Fig. 6.1-b. Any winding configuration can be emulated by connecting slots in series or parallel. Toroidal windings are utilized because they are more flexible in pole-changing applications than conven-

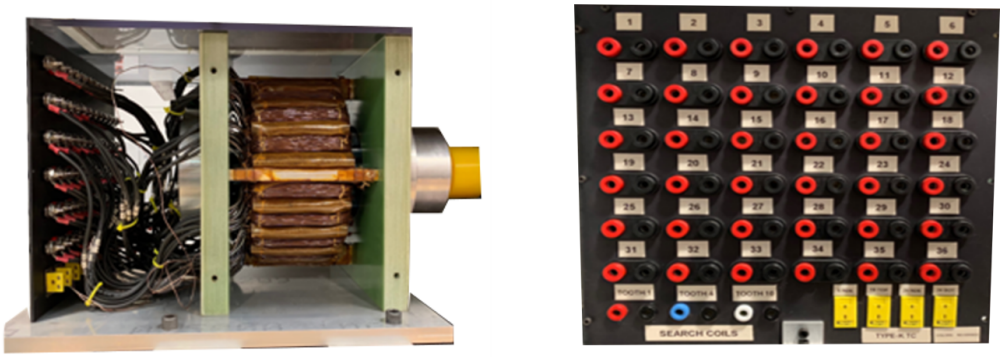

a) Machine side view b) Individual slot access

Figure 6.1: 36-slot toroidally wound IM with external access to each of its slot windings. Each machine slot can be externally accessed through the 72-terminals shown in (b) [14].

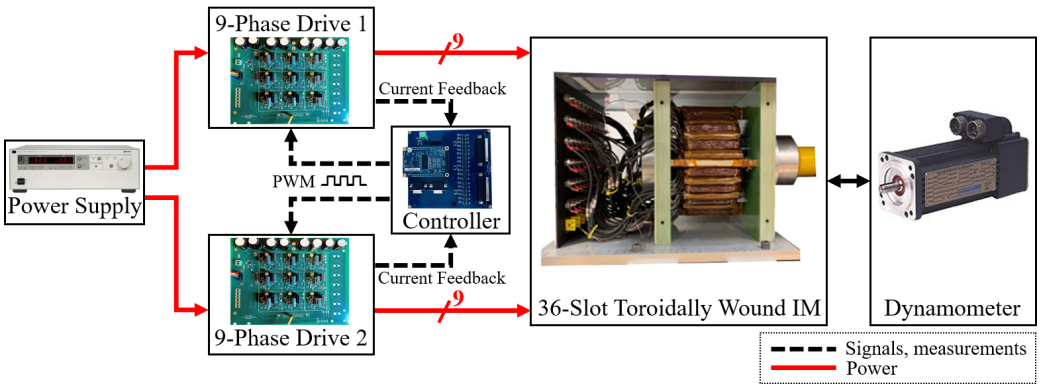

Figure 6.2: Experimental setup. A 36-slot toroidally wound IM is driven by two 9-phase GaN-based inverter modules. The control board commands the inverter excitation pattern and varies the IM pole count.

tional single- or double-layer windings. In single- or double-layer windings, the return path of each slot coil is forced through another slot, which reduces the number of independent currents and constrains pole changing. The return path of a toroidal coil is placed on top of the slot and does not impose any constraint on other slot currents. Figure 6.2 shows the experimental setup. The machine is driven by a GaN-based 18-port inverter consisting of

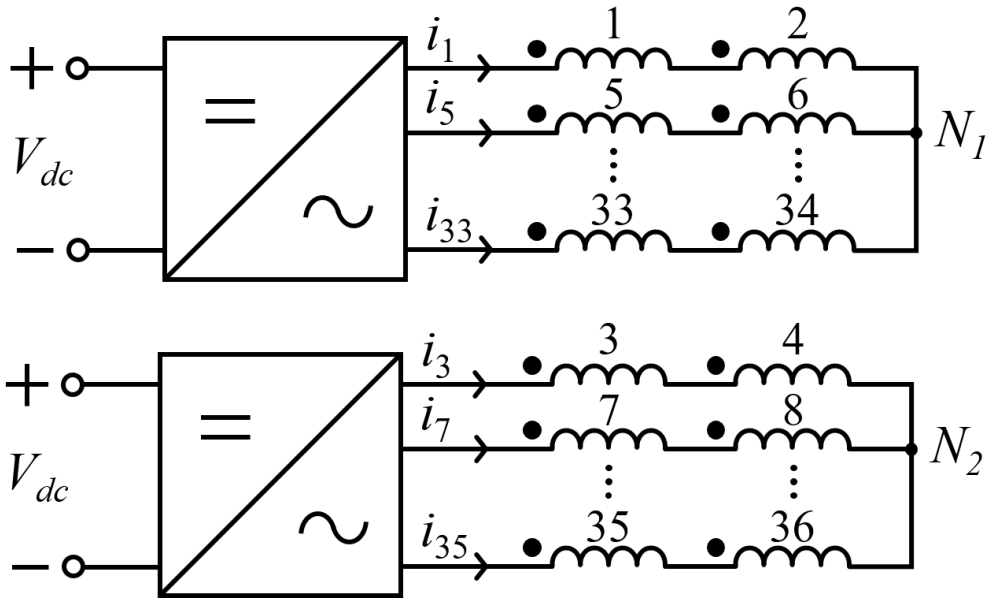

Figure 6.3: Inverter modules and machine configuration schematic. Each index difference of "1" corresponds to 10° mechanical angle between the physical windings. Both inverters are fed from the same dc bus.

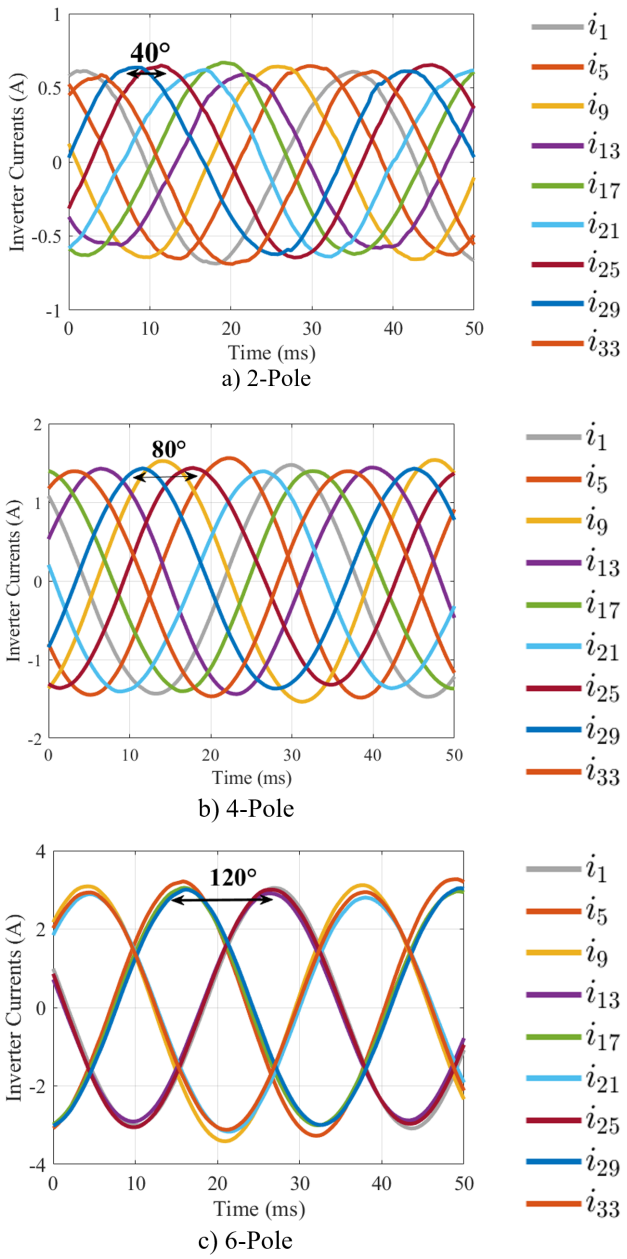

Figure 6.4: Experimental no-load currents of one 9-leg module for (a) 2-pole, (b) 4-pole and (c) 6-pole operation at the same V/ω_e ratio of 0.025 Wb-t. The double arrow marks the electrical phase shift between two consecutive inverter legs, spaced by 40° mechanically. The electrical phase shift is proportional to the pole count.

two identical 9-phase modules. GaN Transphorm TP65H035WS devices are used. Every pair of adjacent machine slots is connected in series to match the number of stator terminals with inverter ac ports. The experimental

machine and drive configuration is equivalent to having an 18-slot IM with control of each slot current, as shown in Fig. 2.1. The control PCB processes 18 differential current measurements and converts them to single-ended analog inputs. Three analog multiplexers interface 18 current measurements with the Cyclone DE0-Nano FPGA, which has 8 analog channels. RC filters are used to reduce measurement noise. FPGA commands the pole count and voltage and transmits PWM signals to each 9-phase unit. A dynamometer loads the IM and is controlled using LabVIEW to command the load torque. The machine speed, torque, and output power are determined via LabVIEW. The instantaneous and average machine input power (drive output power) are computed in the control board using the 18-phase current measurements and reference voltages. Table 6.1 provides experimental machine dimensions and testing limits.

Figure 6.3 shows the inverter and machine connection schematic. Every pair of adjacent machine slots is externally connected in series through the accessible terminals, shown in Fig. 6.1-b. Each inverter connects to slots which are mechanically spaced by 40° to form multiphase balanced loads at 2-, 4- and 6-pole. More modules with fewer ac ports per module is not possible because 6-pole configuration will require single-phase operation in each module. Figure 6.4 shows currents in one 9-leg module at 2-, 4- and 6-pole. The electrical phase shift at 2-pole is equal to the mechanical spacing of 40°. At 4-pole, electrical phase shift is 80°. Three-phase operation with 120° phase shift leads to 6-pole operation.

Table 6.1: Experimental machine dimensions and testing limits

Quantity	**Value**
Per-Slot voltage limit (V)	10
Per-Slot current limit (A)	4.5
Flux-linkage limit (Wb-t)	0.036
Total number of stator slots, Q_s	36
Airgap, g (mm)	0.6
Rotor radius, r (mm)	50
Stack length, l (mm)	71
Number of turns-per-slot, N	46

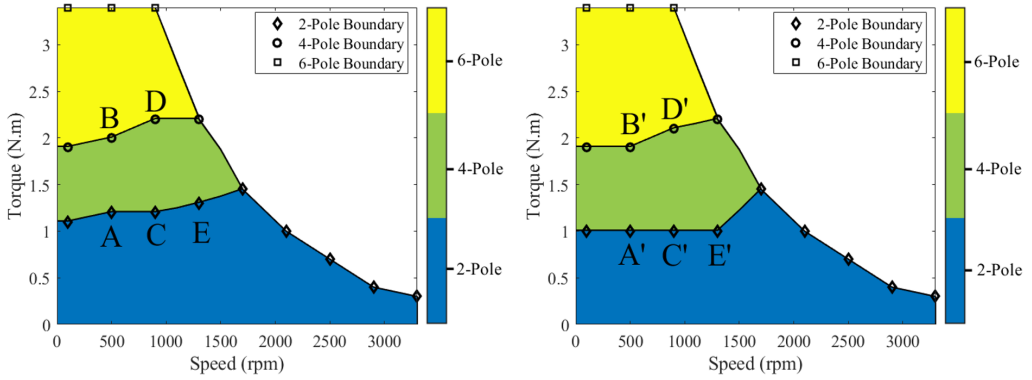

(a) MTPA (b) Minimum Loss Operation

Figure 6.5: Experimental (a) MTPA and (b) minimum loss operation colormaps. Experimental tests were done at speeds ranging from 100 to 3300 rpm with a step size of 400 rpm. The boundary points are linearly connected to generate the experimental optimal region for each pole count.

6.2 Experimental Results: Loss Minimization and MTPA

This section provides experimental results to validate the proposed pole selection methods. Figure 6.5 shows the experimental optimal pole colormaps based on MTPA and minimum-loss operation. The boundary region of each pole count is obtained by experimenting at speeds ranging from 100 to 3300 rpm, with a step size of 400 rpm. At speeds below 900 rpm, pole count is gradually shifted from 2- to 4- to 6-pole as torque increases from 0.1 to 3.3 N·m. Lower pole counts are preferred over 6-pole to produce light and intermediate torque. At high speeds, higher pole counts are constrained by the inverter voltage and must be flux weakened. Beyond 1700 rpm, 6- and 4-pole are in deep flux weakening and lose their torque capability. Thus, a 2-pole configuration is used for any speed beyond 1700 rpm. Figures 6.6-6.7 show the experimental torque-per-ampere and machine power losses at four different speeds (500, 900, 1300 and 1700 rpm). At 500 and 900 rpm, the torque-per-ampere and power losses of successive pole counts intersect at the pole transition points A to D and A' to D'. Losses and torque-per-ampere of 2- and 4- pole are better than 6-pole at light and intermediate torque values. Using 6-pole is only justified at high torque levels and low speeds. Beyond 1300 rpm, the 6-pole count has higher losses and current than all other configurations due to deep flux weakening. At these high speeds, 6-pole must

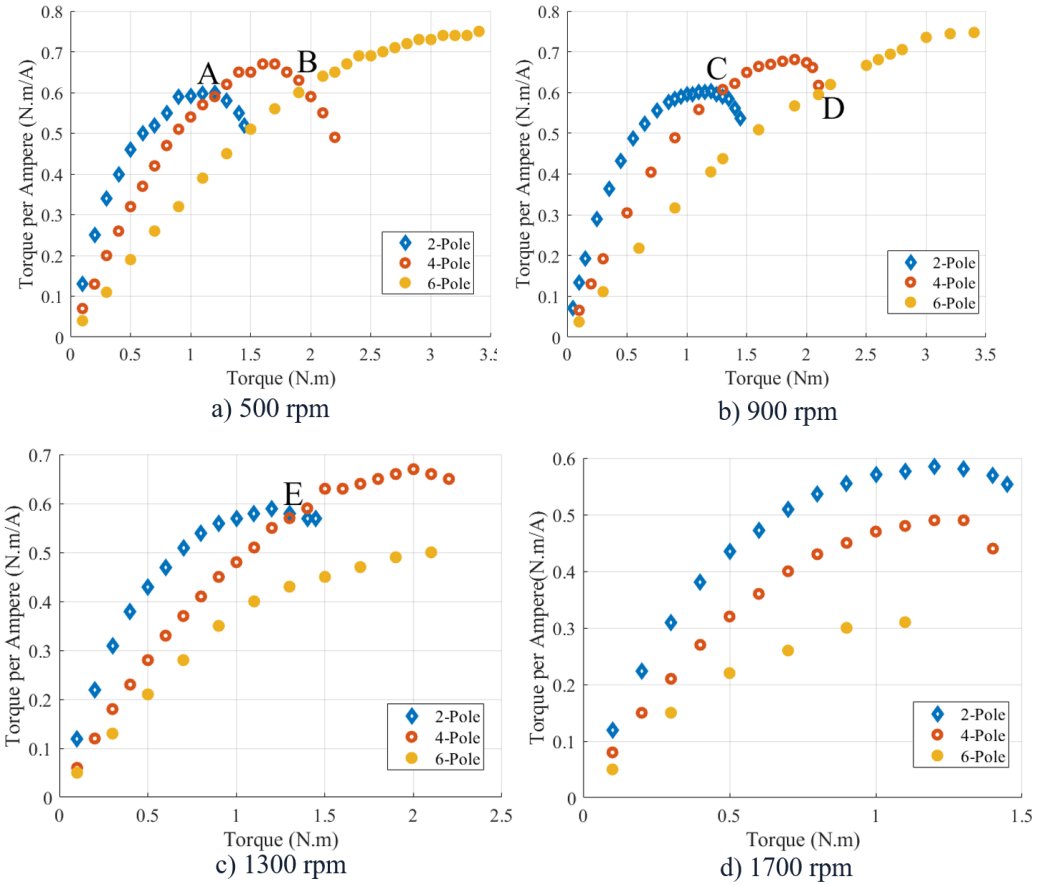

Figure 6.6: Experimental torque-per-ampere as a function of torque for different pole configurations at speeds of (a) 500 rpm, (b) 900 rpm, (c) 1300 rpm and (d) 1700 rpm. The points A, B, C, D and E are the pole transition points marked in Fig. 6.5(a).

make up for its reduced magnetizing current i_{ds} with higher i_{qs}, which leads to a drop of its torque-per-ampere and increase in power losses. At 1300 rpm, pole count is varied from 2- to 4-pole at points E and E'. At 1700 rpm, 2-pole has higher torque-per-ampere and smaller power losses at all torque levels, and thus it is used regardless of the torque level. Experimental results validate that pole selection should be based on both torque and speed to minimize machine losses and stator current.

Figure 6.8 shows power loss reduction and torque-per-ampere improvement achieved by using the proposed pole selection method compared to linking the pole count only to the machine operating speed. In conventional speed-based pole selection approaches, 6-pole is used below 1300 rpm, 4-pole is used between 1300 and 1700 rpm, and 2-pole is used beyond 1700

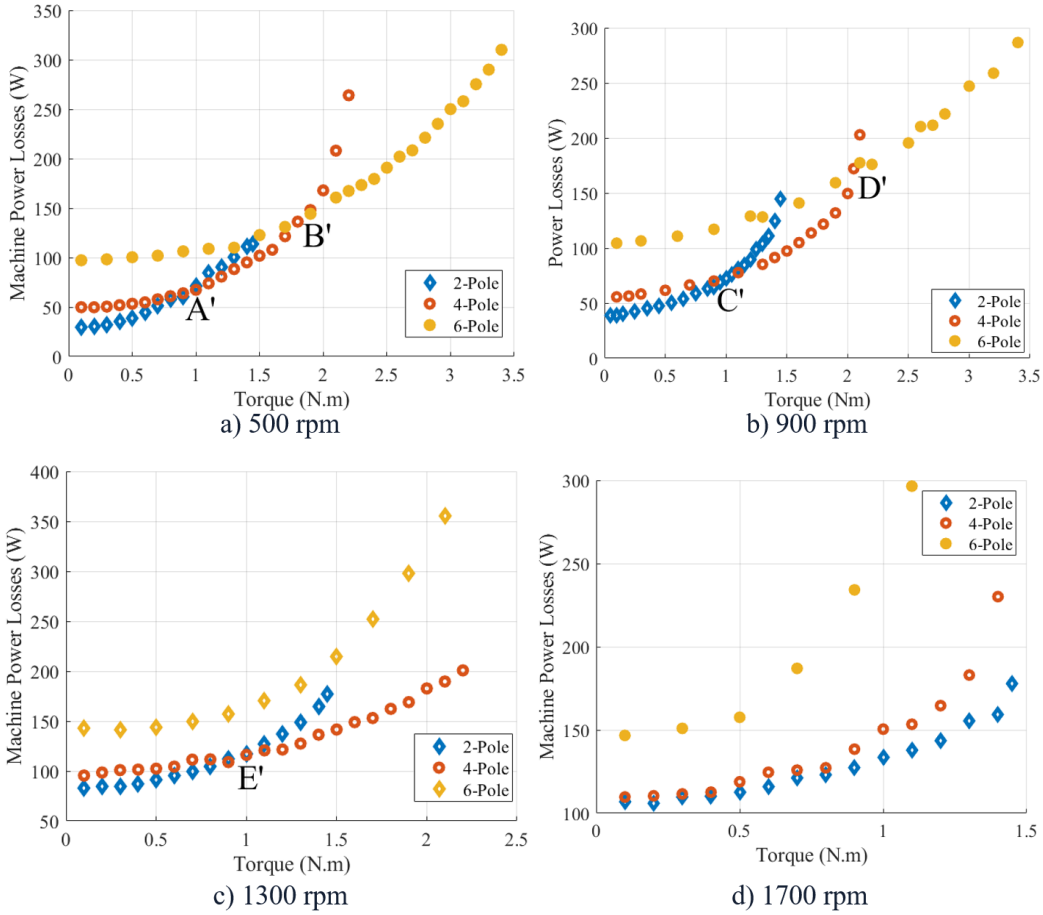

Figure 6.7: Experimental power losses as a function of torque for different pole configurations at speeds of (a) 500 rpm, (b) 900 rpm, (c) 1300 rpm and (d) 1700 rpm. The points A', B', C', D' and E' are the pole transition points marked in Fig. 6.5(b).

rpm. Conventional pole selection method does not consider the torque required when selecting pole count. In our proposed pole-selection methods, higher pole counts are only used when a high torque is required and lower pole counts are favored to produce light and intermediate torque. Power loss and torque-per-ampere reductions are most significant at partial loads. This is because the proposed methods select lower pole counts under partial loading conditions, whereas conventional methods select the pole count with the highest torque capability. Near rated conditions, improvements of the proposed method become zero as both methods yield the same pole count selection. The proposed method improves efficiency, reduces stator current at partial loads and maintains the same losses as conventional methods near

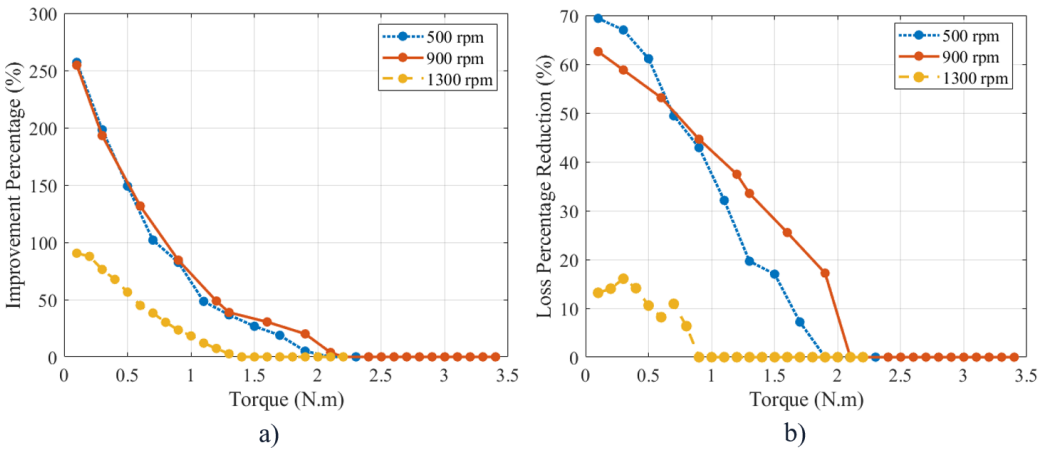

Figure 6.8: (a) Torque-per-ampere percentage improvement and (b) power losses percentage reduction as function of torque (N·m) when comparing the proposed MTPA and loss minimization approaches with conventional speed-linked pole selection methods. Improvements are most significant under partial loading conditions and converge to 0 at high loads as both methods yield the same pole count selection near rated conditions.

rated condition. Average torque-per-ampere improvements of 2X and power loss reduction by 1/3 are experimentally achieved when partial torques are produced.

6.3 Experimental Results: Power Electronics Drive

Drive power losses for 2- and 4-pole are shown in Fig 6.9 as torque is increased from 0.1 to 2.1 N·m at 900 rpm. The power electronics converter operates more efficiently with a 2-pole configuration at partial torques (lower than 1.1 N·m). Beyond 1.1 N·m, the converter is more efficient when 4-pole is used. MTPA and minimum loss operation minimize the stator current and power processed by the drive. Thus, using the proposed pole selection methods not only minimizes machine losses, but also reduces power electronics losses. Figure 6.10 shows the worst case dc bus voltage ripple of one of the 9-leg modules for 2- and 6-pole. The load current, switching frequency and capacitance values are the same for both 2- and 6-pole. As shown in Fig. 6.4, the currents in a 9-leg module form a 9-phase pattern at 2-pole, and a repeating 3-phase pattern at 6-pole. The 6-pole configuration has 2.6 times more voltage ripple compared to 2-pole as it uses three-phase.

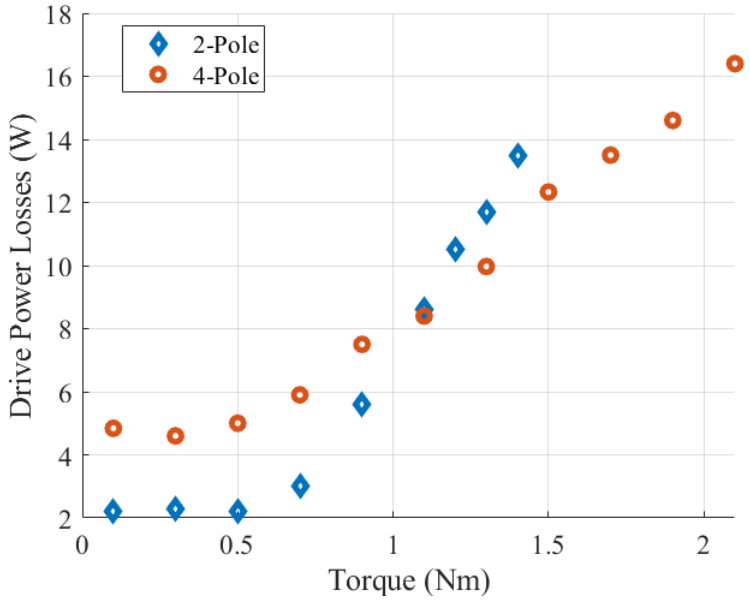

Figure 6.9: Experimental drive power losses (W) versus IM torque at a speed of 900 rpm when the machine is configured as 2- and 4-pole. Variable-pole operation minimizes the drive power losses under all operating conditions.

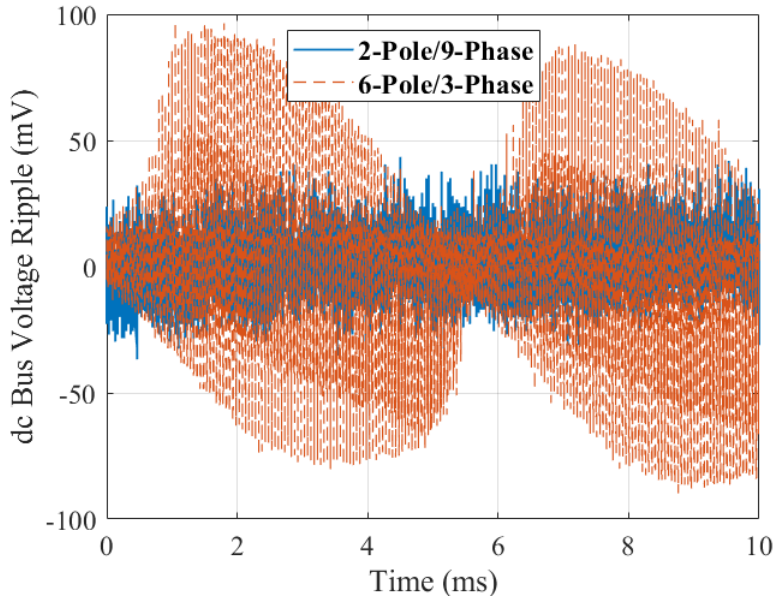

Figure 6.10: Experimental dc bus voltage ripple (mV) at 2-pole/9-phase and 6-pole/3-phase. The ceramic capacitance is 54 µF and the electrolytic capacitance is 0.8 mF. The load current is 2.51 A in both cases. The switching frequency is 20 kHz. The 6-pole configuration requires three-phase operation and has larger voltage ripple.

CHAPTER 7

CONCLUSION AND FUTURE WORK

7.1 Conclusion

Electronically varying the IM pole count can be exploited to minimize drivetrain losses in dynamic applications like EVs. Conventionally, variable-pole IMs were used to extend the machine speed range by using high pole counts at low speeds and low pole count at high speeds. Pole selection was solely based on the operating speed. In this thesis, we extended pole-selection strategies for variable-pole IMs to consider both torque and speed. Lower pole counts minimize magnetizing current and core losses and are more efficient at producing light and intermediate torques. High pole counts are only used when high torque is required. Experimental loss reduction and torque-per-ampere improvement of $1/3$ and $2X$ were achieved at partial loading by utilizing the proposed pole-selection method, rather than just selecting pole count with highest torque capability at a given operating speed. Losses are most significantly reduced at partial loading, where an EV drivetrain operates for the predominant period of the drive cycle. This thesis also discussed the design of modular multiphase drives for EVs. In addition to providing the flexibility to vary IM pole count, modular multiphase drives are more efficient and compact than conventional 3-phase drives. A power electronics converter with 18 ac ports has roughly half the losses of a 3-phase drive and can decrease dc link capacitor power and energy ratings. This thesis work opens up the opportunity to design cost effective, energy efficient and compact rare-earth-free EV drivetrains.

7.2 Future Work

Possible future work may include the following:

- Compare energy efficiency of variable-pole IM for EVs with fixed-pole IMs and PM motors.
- Co-design IM and power electronics drive. Conventionally, electric machine and drive are designed independently. In this thesis work, we showed that variable-pole IMs and their modular multiphase drives are extremely interdependent. A generalized framework was provided to model the impact of machine on power electronics. In the future, a co-design of both variable-pole IM and its power electronics will be done to achieve high system-level efficiency and power density.
- Investigate transient and dynamic performance. A smooth on-the-fly pole count transition will be done. Drive cycle simulations may be done to investigate how variable-pole IMs perform in real driving scenarios.

REFERENCES

[1] United States Environmental Protection Agency, "Fast facts on transportation greenhouse gas emissions." [Online]. Available: https://www.epa.gov/greenvehicles/fast-facts-transportation-greenhouse-gas-emissions

[2] A. Poullikkas, "Sustainable options for electric vehicle technologies," *Renewable and Sustainable Energy Reviews*, vol. 41, pp. 1277 – 1287, 2015. [Online]. Available: http://www.sciencedirect.com/science/article/pii/S1364032114007898

[3] Q. Qiao, F. Zhao, Z. Liu, X. He, and H. Hao, "Life cycle greenhouse gas emissions of Electric Vehicles in China: Combining the vehicle cycle and fuel cycle," *Energy*, vol. 177, pp. 222 – 233, 2019. [Online]. Available: http://www.sciencedirect.com/science/article/pii/S0360544219307133

[4] Edision Electric Institute, "Electric vehicle sales: Facts and figures." [Online]. Available: https://www.eei.org/issuesandpolicy/electrictransportation/Documents

[5] A. M. Bazzi, Y. Liu, and D. S. Fay, "Electric machines and energy storage: Over a century of technologies in electric and hybrid electric vehicles," *IEEE Electrification Magazine*, vol. 6, no. 3, pp. 49–53, 2018.

[6] J.-R. Riba, C. López-Torres, L. Romeral, and A. Garcia, "Rare-earth-free propulsion motors for electric vehicles: A technology review," *Renewable and Sustainable Energy Reviews*, vol. 57, pp. 367 – 379, 2016.

[7] United States Department of Energy, "US drive electrical and electronics technical team roadmap." [Online]. Available: https://www.energy.gov/eere/vehicles/downloads/us-drive-electrical-and-electronics-technical-team-roadmap

[8] Economic Times, "High efficiency gains to spur use of PM motor in future EV designs: Report." [Online]. Available: https://auto.economictimes.indiatimes.com/news/auto-components/high-efficiency-gains-to-spur-use-of-pm-motor-in-future-ev-designs-report/72317517

[9] W. Zhao, T. A. Lipo, and B. Kwon, "Comparative study on novel dual stator radial flux and axial flux permanent magnet motors with ferrite magnets for traction application," *IEEE Transactions on Magnetics*, vol. 50, no. 11, pp. 1–4, 2014.

[10] K. Rajashekara, "History of electric vehicles in general motors," *IEEE Transactions on Industry Applications*, vol. 30, no. 4, pp. 897–904, 1994.

[11] V. T. Buyukdegirmenci, A. M. Bazzi, and P. T. Krein, "Evaluation of induction and permanent-magnet synchronous machines using drive-cycle energy and loss minimization in traction applications," *IEEE Transactions on Industry Applications*, vol. 50, no. 1, pp. 395–403, 2014.

[12] Z. Yang, F. Shang, I. P. Brown, and M. Krishnamurthy, "Comparative Study of Interior Permanent Magnet, Induction, and Switched Reluctance Motor Drives for EV and HEV Applications," *IEEE Transactions on Transportation Electrification*, vol. 1, no. 3, pp. 245–254, 2015.

[13] Roskill, "Rare Earths: Audi opting for induction motor technology in its e-tron EV." [Online]. Available: https://roskill.com/news/rare-earths-audi-opting-for-induction-motor-technology-in-its-e-tron-ev/

[14] M. Magill, "An investigation of electronic pole changing in high inverter count induction machines." Technical Report UILU-ENG2015-2505, CEME-TR-2015-01, April 2015.

[15] M. Osama and T. A. Lipo, "A new inverter control scheme for induction motor drives requiring wide speed range," *IEEE Transactions on Industry Applications*, vol. 32, no. 4, pp. 938–944, July 1996.

[16] J. M. Miller, V. Stefanovic, V. Ostovic, and J. Kelly, "Design considerations for an automotive integrated starter-generator with pole-phase modulation," in *Conference Record of the 2001 IEEE Industry Applications Conference. 36th IAS Annual Meeting (Cat. No.01CH37248)*, vol. 4, 2001, pp. 2366–2373 vol.4.

[17] A. Harson, P. H. Mellor, and D. Howe, "Design considerations for induction machines for electric vehicle drives," in *1995 Seventh International Conference on Electrical Machines and Drives (Conf. Publ. No. 412)*, 1995, pp. 16–20.

[18] A. B. Jidin, N. R. B. N. Idris, A. H. B. M. Yatim, M. E. Elbuluk, and T. Sutikno, "A wide-speed high torque capability utilizing overmodulation strategy in DTC of induction machines with constant switching frequency controller," *IEEE Transactions on Power Electronics*, vol. 27, no. 5, pp. 2566–2575, 2012.

[19] M. Osama and T. A. Lipo, "Modeling and analysis of a wide-speed-range induction motor drive based on electronic pole changing," *IEEE Transactions on Industry Applications*, vol. 33, no. 5, pp. 1177–1184, 1997.

[20] M. P. Magill, P. T. Krein, and K. S. Haran, "Equivalent circuit model for pole-phase modulation induction machines," in *2015 IEEE International Electric Machines Drives Conference (IEMDC)*, 2015, pp. 293–299.

[21] B. S. Umesh and K. Sivakumar, "Dual-inverter-fed pole-phase modulated nine-phase induction motor drive with improved performance," *IEEE Transactions on Industrial Electronics*, vol. 63, no. 9, pp. 5376–5383, 2016.

[22] S. Günther, S. Ulbrich, and W. Hofmann, "Driving cycle-based design optimization of interior permanent magnet synchronous motor drives for electric vehicle application," in *2014 International Symposium on Power Electronics, Electrical Drives, Automation and Motion*, 2014, pp. 25–30.

[23] B. Bilgin, P. Magne, P. Malysz, Y. Yang, V. Pantelic, M. Preindl, A. Korobkine, W. Jiang, M. Lawford, and A. Emadi, "Making the case for electrified transportation," *IEEE Transactions on Transportation Electrification*, vol. 1, no. 1, pp. 4–17, 2015.

[24] E. Libbos, B. Ku, S. Agrawal, S. Tungare, A. Banerjee, and P. T. Krein, "Variable-pole induction machine drive for electric vehicles," in *2019 IEEE International Electric Machines Drives Conference (IEMDC)*, May 2019, pp. 515–522.

[25] E. Libbos and B. Ku and S. Agrawal and S. Tungare and A. Banerjee and P. T. Krein, "Loss minimization and maximum torque per ampere operation for variable-pole induction machines," *IEEE Transactions on Transportation Electrification*, (Accepted).

[26] E. Libbos, R. Hao, B. Ku, A. Banerjee, and P. T. Krein, "Modular multiphase drives for variable-pole induction machines in electric vehicles," in *2020 IEEE Applied Power Electronics Conference (APEC)*, (Accepted).

[27] P. L. Alger, *The Nature of Polyphase Induction Machines*. New York: Wiley, 1951.

[28] V. Ostovic, "Pole-changing permanent-magnet machines," *IEEE Transactions on Industry Applications*, vol. 38, no. 6, pp. 1493–1499, 2002.

[29] E. Levi, R. Bojoi, F. Profumo, H. A. Toliyat, and S. Williamson, "Multiphase induction motor drives - a technology status review," *IET Electric Power Applications*, vol. 1, no. 4, pp. 489–516, 2007.

[30] P. T. Krein, R. S. Balog, and M. Mirjafari, "Minimum energy and capacitance requirements for single-phase inverters and rectifiers using a ripple port," *IEEE Transactions on Power Electronics*, vol. 27, no. 11, pp. 4690–4698, 2012.

[31] T. A. Lipo, *Introduction to AC Machine Design*. John Wiley & Sons, 2017.

[32] F. Liang, D. W. Novotny, R. W. Fei, and X. Xu, "Selection of the pole number of induction machines for variable speed applications," *IEEE Transactions on Industry Applications*, vol. 31, no. 2, pp. 304–310, 1995.

[33] W. Leonhard, *Control of Electrical Drives*. Springer Science & Business Media, 2001.

[34] C. P. Steinmetz, "On the law of hysteresis," *Proceedings of the IEEE*, vol. 72, no. 2, pp. 197–221, 1984.

[35] S. Bozhko, S. Dymko, S. Kovbasa, and S. M. Peresada, "Maximum torque-per-amp control for traction im drives: Theory and experimental results," *IEEE Transactions on Industry Applications*, vol. 53, no. 1, pp. 181–193, 2016.

[36] O. Wasynczuk, S. Sudhoff, K. Corzine, J. L. Tichenor, P. Krause, I. Hansen, and L. Taylor, "A maximum torque per ampere control strategy for induction motor drives," *IEEE Transactions on Energy Conversion*, vol. 13, no. 2, pp. 163–169, 1998.

[37] R. J. Kerkman, "Steady-state and transient analyses of an induction machine with saturation of the magnetizing branch," *IEEE Transactions on Industry Applications*, vol. IA-21, no. 1, pp. 226–234, 1985.

[38] J. Wang, Y. Li, and Y. Han, "Integrated modular motor drive design with gan power fets," *IEEE Transactions on Industry Applications*, vol. 51, no. 4, pp. 3198–3207, 2015.

[39] T. M. Jahns and H. Dai, "The past, present, and future of power electronics integration technology in motor drives," *CPSS Transactions on Power Electronics and Applications*, vol. 2, no. 3, pp. 197–216, 2017.

[40] Rohm Semiconductor, "SiC BSM300D12P2E001 Datasheet." [Online]. Available: https://www.rohm.com/products/sic-power-devices/sic-power-module/bsm300d12p2e001-product

[41] Cree Inc., "SiC C2M0040120D Datasheet." [Online]. Available: {https://www.wolfspeed.com/downloads/dl/file/id/165/product/9/c2m0040120d.pdf}

[42] Transphorm, "GaN TP65H035WSQA Datasheet." [Online]. Available: https://www.transphormusa.com/en/product/tp65h035wsqa/

[43] H. Wen, W. Xiao, X. Wen, and P. Armstrong, "Analysis and evaluation of dc-link capacitors for high-power-density electric vehicle drive systems," *IEEE Transactions on Vehicular Technology*, vol. 61, no. 7, pp. 2950–2964, 2012.

[44] M. Vujacic, O. Dordevic, and G. Grandi, "Evaluation of dc-link voltage switching ripple in multiphase pwm voltage source inverters," *IEEE Transactions on Power Electronics*, vol. 35, no. 4, pp. 3478–3490, 2020.

APPENDIX A

9-PHASE INVERTER PCB LAYOUT

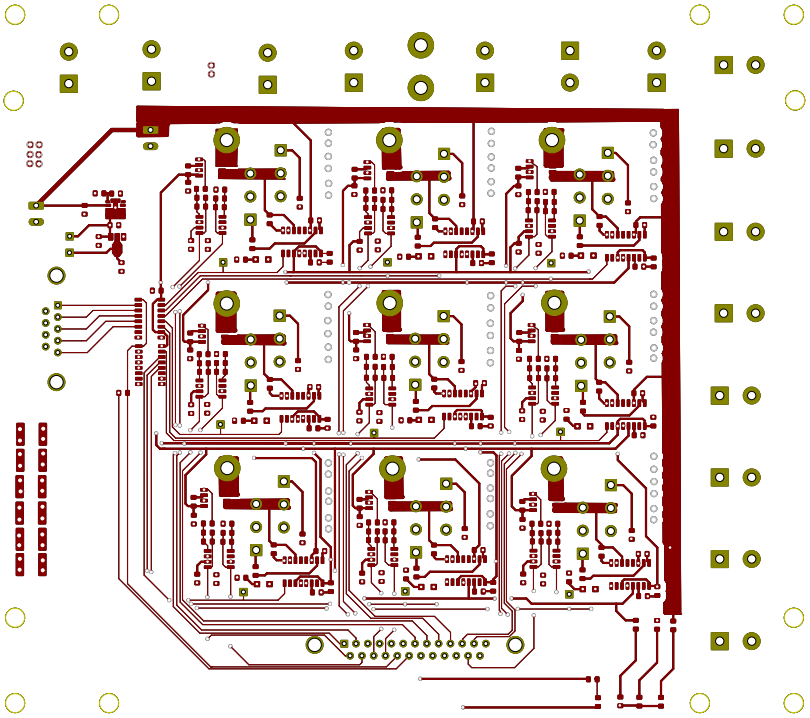

Figure A.1: 9-phase inverter module PCB top layer layout.

APPENDIX B

9-PHASE INVERTER PCB: TOP VIEW

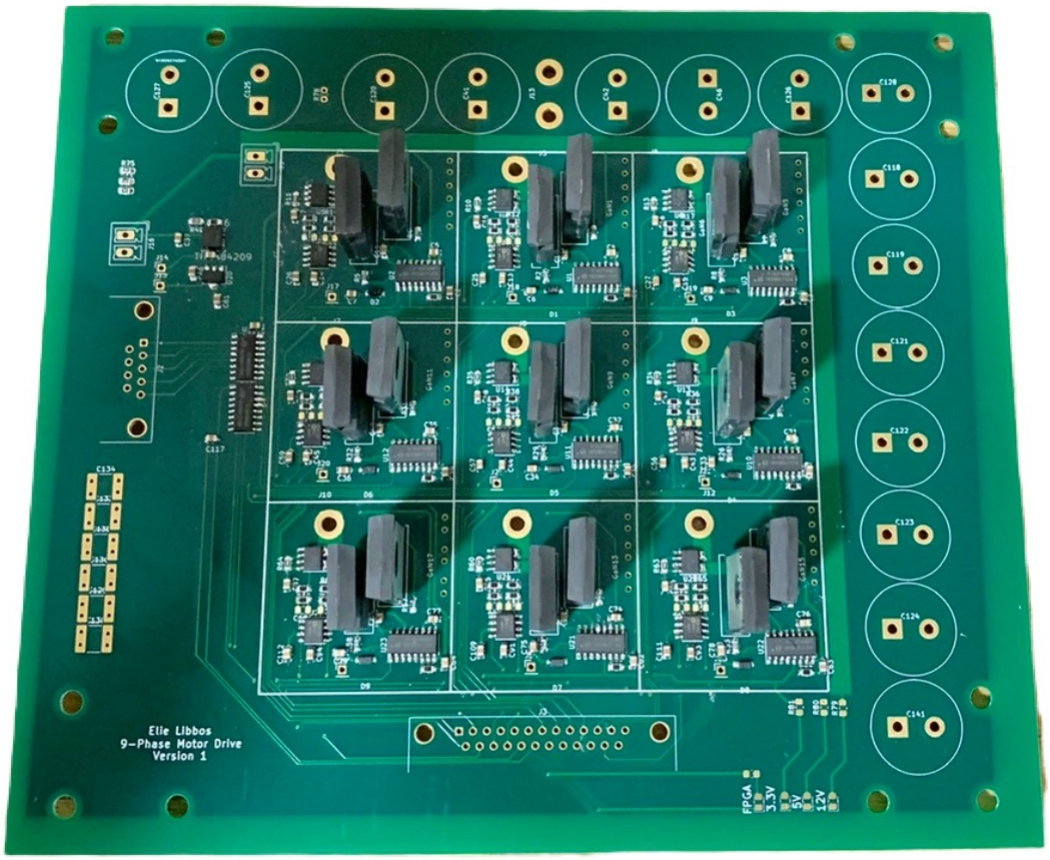

Figure B.1: Top view of 9-phase inverter module.

APPENDIX C

CONTROL BOARD PCB LAYOUT

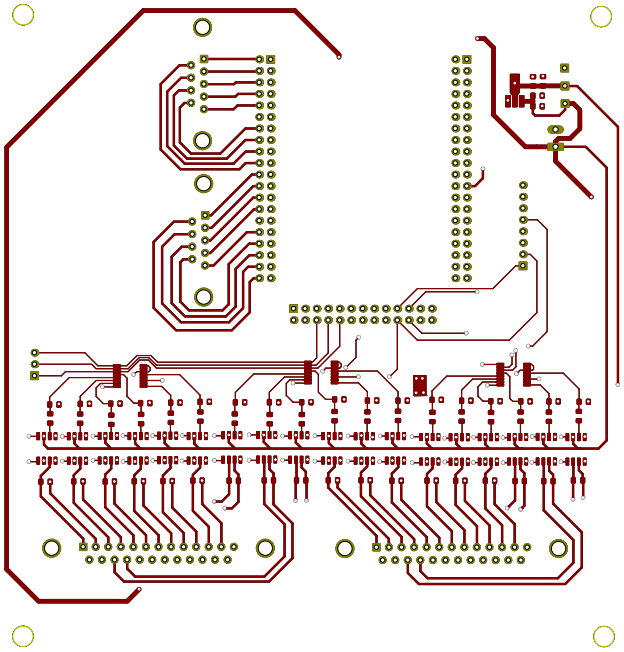

Figure C.1: Control board PCB top layer layout.

APPENDIX D

CONTROL BOARD PCB: TOP VIEW

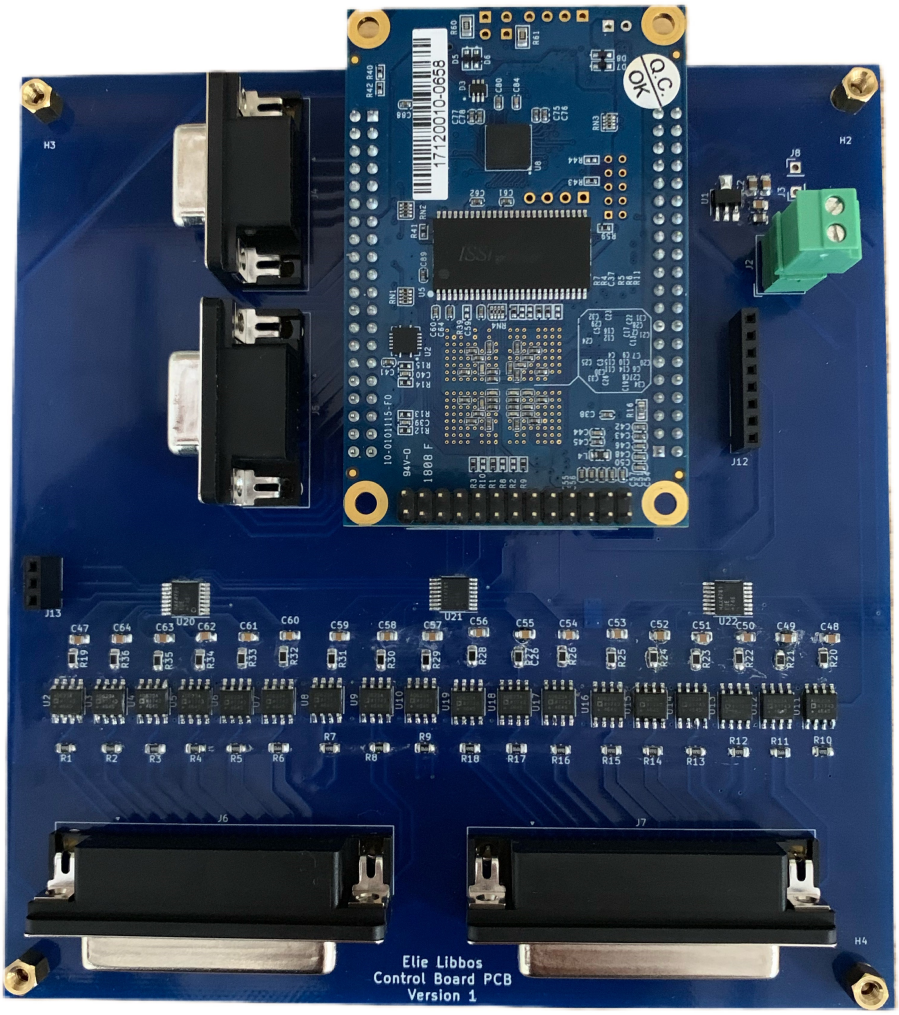

Figure D.1: Top view of control board PCB.